

21



(NASA-CR-120374) DESIGN AND TESTING OF
A TANDEM ROW PUMP INDUCER (Hydronautics,
Inc.) 10~~9~~ p HC \$8.50 CSCL 13K

///

67324252677
N74-30921
Unclas
G3/15 17004
67324252677

HYDRONAUTICS, incorporated research in hydrodynamics

Research, consulting, and advanced engineering in the fields of NAVAL
and INDUSTRIAL HYDRODYNAMICS. Offices and Laboratory in the
Washington, D. C. area: Pindell School Road, Howard County, Laurel, Md.

HYDRONAUTICS, Incorporated

TECHNICAL REPORT 7117-1

DESIGN AND TESTING OF A
TANDEM ROW PUMP INDUCER

By

Robert J. Etter

March 1974

Prepared for

National Aeronautics and Space Administration
George C. Marshall Space Flight Center
Huntsville, Alabama

Under
Contract No. NAS8-26591

REPORT DOCUMENTATION PAGE		READ INSTRUCTIONS BEFORE COMPLETING FORM
1. REPORT NUMBER T. R. 7117-1	2. GOVT ACCESSION NO.	3. RECIPIENT'S CATALOG NUMBER
4. TITLE (and Subtitle) DESIGN AND TESTING OF A TANDEM ROW PUMP INDUCER		5. TYPE OF REPORT & PERIOD COVERED Technical Report
7. AUTHOR(s) Robert J. Etter		6. PERFORMING ORG. REPORT NUMBER T. R. 7117-1
9. PERFORMING ORGANIZATION NAME AND ADDRESS HYDRONAUTICS, Incorporated 7210 Pindell School Road, Howard County, Laurel, Maryland 20810		8. CONTRACT OR GRANT NUMBER(s) NAS8-26591
11. CONTROLLING OFFICE NAME AND ADDRESS National Aeronautics and Space Administration, George C. Marshall Space Flight Cen. Huntsville, Alabama		10. PROGRAM ELEMENT, PROJECT, TASK AREA & WORK UNIT NUMBERS
14. MONITORING AGENCY NAME & ADDRESS (if different from Controlling Office)		12. REPORT DATE March 1974
		13. NUMBER OF PAGES 107
		15. SECURITY CLASS. (of this report) Unclassified
		15a. DECLASSIFICATION/DOWNGRADING SCHEDULE None
16. DISTRIBUTION STATEMENT (of this Report)		
17. DISTRIBUTION STATEMENT (of the abstract entered in Block 20, if different from Report)		
18. SUPPLEMENTARY NOTES		
19. KEY WORDS (Continue on reverse side if necessary and identify by block number) Inducers Pumps Supercavitating Inducers Tandem Inducers		
20. ABSTRACT (Continue on reverse side if necessary and identify by block number) The design and testing of a tandem row pump inducer having a supercavitating first stage with a 0.60 hub ratio is presented. The second stage tested was a helical impeller with a 0.70 hub ratio. A cubic arc transition was utilized to accomplish the hub change. The first stage had two blades and the free-vortex design approach was empirically modified based on previous experience.		

UNCLASSIFIED

SECURITY CLASSIFICATION OF THIS PAGE(When Data Entered)

20. Cont.

The recommended second stage design having four blades and using cambered blade sections is presented but the model was not built or tested. The more simple helix was built instead to reduce cost. Data taken included head generation, cavitation observations and unsteady head fluctuations over the 0-100 Hz range.

ib

UNCLASSIFIED

SECURITY CLASSIFICATION OF THIS PAGE(When Data Entered)

TABLE OF CONTENTS

	Page
ABSTRACT.....	1
1.0 INTRODUCTION.....	2
2.0 GENERAL COMMENTS REGARDING MODELING AND SUCTION SPECIFIC SPEED.....	7
3.0 BACKGROUND.....	11
4.0 INDUCER DESIGN.....	17
General Considerations.....	17
First Stage Design.....	19
Transition Design.....	28
Second Stage Design.....	30
5.0 TEST FACILITY AND PROCEDURE.....	41
6.0 TEST RESULTS AND DISCUSSION.....	44
7.0 CONCLUSIONS.....	54
REFERENCES.....	57

LIST OF FIGURES

- Figure 1 - Influence of Flow Coefficient on Relationship Between Suction Specific Speed and Tip Cavitation Number for a 0.60 Hub/Diameter Ratio
- Figure 2 - Influence of Hub/Diameter Ratio and Flow Coefficient on Suction Specific Speed at $\sigma_t = 0.010$.
- Figure 3 - First Stage Impeller Sections - Full Scale
- Figure 4 - Three Views of the Supercavitating Stage Having Five-Term Cambered Blade Forms, Constant Chord Length and a 60% Hub Ratio
- Figure 5 - First Stage (Supercavitating) Impeller
- Figure 6 - Multiple Milling of Impeller Blades from Pattern
- Figure 7 - Non-Dimensional Comparison of Leading and Trailing Edge Profiles Used in Saturn V Engine Inducers to 5-Term Cambered Model with Constant Chord Length (Wrap Not Properly Indicated)
- Figure 8 - Cubic Arc Transition Shape
- Figure 9 - Cubic Arc Transition Section
- Figure 10 - Sample Interference Streamline Calculation Using Both Two and Three Dimensional Results
- Figure 11 - Second Stage Two Dimensional Blade Profiles at Three Radii. (Four Blades, 0.70 Hub)
- Figure 12 - Second Stage Impeller Using Four Blades and 0.70 Hub
- Figure 13 - Second Stage Detail
- Figure 14 - Second Stage (Subcavitating) Impeller

- Figure 15 - Two Stage Inducer Assembly
- Figure 16 - Pump Loop Instrumentation, Control, and Data Acquisition Systems
- Figure 17 - Pump Loop Test Section
- Figure 18 - Yaw Head Probe and Traverse Stand
- Figure 19 - First Stage Head Coefficient As Influenced By Suction Specific Speed and Flow Coefficient
- Figure 20 - First Stage Head Coefficient-Flow Coefficient Relationship for Various Suction Specific Speeds
- Figure 21 - Second Stage Head Coefficient As Influenced By First Stage Suction Specific Speed and Flow Coefficient
- Figure 22 - Second Stage Head Coefficient-Flow Coefficient Relationship for Various First Stage Suction Specific Speeds
- Figure 23 - Tandem Head Coefficient As Influenced By Suction Specific Speed and Flow Coefficient
- Figure 24 - Tandem Head Coefficient-Flow Coefficient Relationship
- Figure 25 - First Stage Suction Performance Compared to Other Supercavitating Inducers
- Figure 26 - First Stage Cavity Lengths and Cavitation Patterns
- Figure 27 - Second Stage Cavitation Patterns
- Figure 28 - Influence of Flow Coefficient on Cavitation Patterns at Low Suction Specific Speed

- Figure 29 - Cavitation Patterns at Moderate Suction Specific Speeds
- Figure 30 - Cavitation Patterns at High Suction Specific Speeds
- Figure 31 - Two Views of Cavitation Patterns at $\phi = .089$,
 $N_{ss} = 13,430$ at Two Rotational Orientations about
 90° Apart
- Figure 32 - Alternate Blade Cavitation on Second Stage,
 $\phi = .0745$, $N_{ss} = 20,500$.
- Figure 33 - Ratio of Fluctuating to Steady Head Developed by
Stage 1 as Influenced by Suction Specific Speed
and Flow Coefficient
- Figure 34 - Influence of Cavity Length to Chord Ratio on
Fluctuating Head Generation
- Figure 35 - Low Frequency Fluctuating Head Spectrum
- Figure 36 - Uniformity of Axial Velocity Profile Exiting from
Stage 1 for Varying Flow Coefficient at High
Suction Specific Speed
- Figure 37 - Uniformity of Head Generation with Radius for Stage 1
for Varying Flow Coefficient at High Suction Specific
Speed
- Figure 38 - Uniformity of Axial Velocity Profile Exiting from
Stage 1 for a Wide Range of Suction Specific Speed
at Nearly Constant ϕ
- Figure 39 - Uniformity of Head Generation with Radius for Stage 1
for a Wide Range of Suction Specific Speed at Nearly
Constant ϕ .

Figure 40 - Inducer Blade with Trailing Edge Crack Due to
Cantilevered Model Construction

Figure 41 - Leading Edge Damage to Stage 1

LIST OF TABLES

	Page
Table 1 - Design Parameters Compared to J-2 LOX Inducer...	18
Table 2 - Reference (13) and Present Local Cavitation Numbers at Design Flow and Head Coefficients....	26
Table 3 - Stage 1 Detailed Design Summary, $\varphi_o = 0.10$, 4000 rpm.....	27
Table 4 - Summary of Stage 2 - Four Bladed Design.....	36

ABSTRACT

The design and testing of a tandem row pump inducer having a supercavitating first stage with a 0.60 hub ratio is presented. The second stage tested was a helical impeller with a 0.70 hub ratio. A cubic arc transition was utilized to accomplish the hub change. The first stage had two blades and the free-vortex design approach was empirically modified based on previous experience. The recommended second stage design having four blades and using cambered blade sections is presented but the model was not built or tested. The more simple helix was built instead to reduce cost. Data taken included head generation, cavitation observations and unsteady head fluctuations over the 0-100 Hz range.

1.0 INTRODUCTION

The inlet operating conditions of a pump including inlet net positive suction head, rotative speed, and total discharge may be combined to form the parameter, suction specific speed defined by Equation [1],

$$N_{ss} = \frac{n\sqrt{Q}}{NPSH^{3/4}} \quad [1]$$

Although not dimensionless, this parameter, in common use throughout pumping literature, may be shown by dimensional considerations (1)* to indicate the combination of inlet operating conditions which will give similar flow and cavitation patterns in machines which are geometrically similar. For a given discharge, high suction specific speed pumps result when either rotational speed is increased or inlet NPSH is decreased. Both changes result in significant system weight reductions when the pumps under consideration are being used as fuel or oxidizer pumps in liquid-fueled rocket engine systems (2). Reductions in the propulsion system weight can be utilized for a larger payload which is normally only a small percentage of total vehicle weight.

*Numbers in parentheses refer to references listed after the text.

The three stage Saturn V uses liquid fuels and oxidizers with LOX/hydrocarbon fuel in the first stage and LOX/LH₂ in the second and third stages. By far the largest physical components of such a system are the propellant tanks whose wall thickness is determined primarily by tank pressure (3). Lower propellant tank pressures and therefore, lower pump NPSH allow lower vehicle weight. With higher rotative speeds, the size and weight of the fuel pumps are also reduced and the possible need for speed reduction components between turbines and pumps eliminated.

These weight reductions through the use of lower pressures and higher speeds are not, however, achieved without accompanying technical problems. Requiring the fuel/oxidizer** pumps to operate at high values of suction specific speed results in cavitation of the pump impellers. In ordinary pump experience, an N_{ss} value of 8000 or more results in cavitation causing vibration, noise, impeller damage, and a decrease in discharge and efficiency. The problem of pumping at high N_{ss} has however, been largely alleviated through the use of pre-pumping stages called "inducers" which operate rather satisfactorily even with extensive cavitation. A typical inducer consists of a high solidity, axial flow impeller with a small number of blades. The blade form usually approximates a simple helix. Inducers are generally located immediately upstream of the main fuel pump and

**Sometimes referred to only as fuel pumps.

operate at the same rpm on the same shaft as the main pump rotor. The problems of low efficiency and cavitation damage to the impeller blades are not restrictive in the application of inducers to rocket fuel pumps since the inducer produces only a small percentage of the total head rise of the fuel pump and the operating lifetime of the unit is short enough that little damage can occur.

Even in the case of the "one-time" or non-reusable engine, however, the problem of flow instabilities is very significant as a limiting condition for acceptable inducer operation. Model tests and operating experience (4,5,6,7) have shown that under certain operating conditions the discharge and head rise across an inducer may fluctuate violently resulting in corresponding engine thrust fluctuations. The unsteady motions and accelerations caused by the thrust fluctuations provide an unacceptable environment for delicate equipment and astronaut crews. In addition, low frequency oscillations may occur at or near the structural natural frequency.

One method suggested for reducing or eliminating the instabilities and fluctuating output of the inducer is the use of a tandem row inducer whose first stage operates at the design suction specific speed but delivers only a fraction of the total inducer head rise, thus operating with greater stability. The second stage of the inducer consequently operates at a lower suction specific speed and should also deliver the remaining head rise with greater stability. This concept has been used by other investigators (8,9,10,11).

Previous studies conducted at HYDRONAUTICS (12,13) used the innovation of a tandem row inducer design having a supercavitating (14) first stage. The supercavitating stage is one whose blade form is deliberately designed to produce large stable suction side vapor cavities springing from the blade leading edge and collapsing beyond the trailing edge. The second stage was designed as a high solidity high head axial flow rotor to operate with minimum cavitation.

With regard to the instability problem, an originally postulated theory of rotating stall (15) failed to correlate with the observed instabilities noted in the operation of the inducers of (12 and 13). The conclusion of (13) was that the mechanism for flow instability in the models tested appeared to be related to cascade-cavity interference. When the flow coefficient was below a critical value (dependent on the geometry of each inducer) and the suction specific speed was high enough that the cavity extended back to or slightly beyond the leading edge of the adjacent blade, limit cycle cavity oscillations occurred. In this region it was believed that the cavity-length-head relationship for the impeller might be inherently unstable with the cavity length and head oscillating between fixed boundaries.

While not totally eliminating the unstable region, the tandem inducer configuration with a supercavitating first stage did produce a large "stable" operating range. And it was concluded that tandem inducers using supercavitating first stages

and subcavitating second stages may be designed to operate over a fairly wide range of suction specific speeds (models operated at 10,000 - 30,000 in water) and flow coefficients (models operated at .12 - .07) with pressure fluctuations of less than 10 percent of the head generated.

The more conventional helical inducers generally used, operate as partially cavitating impellers; i.e., the suction surface vapor cavities extend from the leading edge of each blade and terminate before reaching the trailing edge. For this type of operation, in order to develop significant head across the first stage at the ambient pressures (NPSH) required, the cavity length must exceed 30 percent of the chord length based on the theoretical results of References (16) and (17). From the experimental cascade results of Reference (18) it appeared that severe cavity oscillations would occur if the cavity length were greater than 30 percent of the chord. As the pressure in the study of (18) was further reduced and the cavities become larger than the chord, the oscillations ceased. This was in agreement with observations on isolated hydrofoils. It seemed, therefore, for the first stage to produce significant head rise and operate stably it must operate in the supercavitating mode.

A more recent study (19) of the instabilities observed in the J-2 LOX system which uses the more conventional helical inducer blade configuration concluded that the so-called "natural filling frequency" phenomena (20) of the partially cavitating

inducer blades may be the principal physical mechanism present driving the LOX system into resonant oscillations. The study of (19) also considered numerous other possible sources of driving force including LOX pre valve wake or cavitation generated disturbances, propellant utilization (P.U.) system disturbances, inlet duct cavitation, blade passage and cavity passage disturbances, tip clearance flow, and rotating stall or surge related phenomena. With the possible exception of the rotating stall or surge phenomena, none of these items seemed a likely source of disturbance in the frequency or magnitude range required to explain the self-induced oscillations observed. Thus, the further motivation for the study of supercavitating inducers is apparent.

2.0 GENERAL COMMENTS REGARDING MODELING AND SUCTION SPECIFIC SPEED

In the present study, the nominal pumps following the inducers may be axial or centrifugal and cryogenic fuels or oxidizers are being pumped. The properties of cavitating flows in cryogenic fluids are such that modeling the flows in water is a conservative procedure, that is, cavitating flows in cryogenic fluids are more likely to be stable at a given set of operating parameters than flows in water at the same operating parameters. One factor which contributes to the stability of cryogenic cavity flows is local cooling at the cavity boundary (3). This local cooling results in a liquid film at the vapor cavity with a lower vapor pressure than that of the bulk fluid. Reference (3) presents the following equation for this local vapor pressure drop:

$$\Delta P_v = K \left(\frac{\rho_v}{\rho_L} \frac{L}{C_s} \frac{dp}{dT} \right) \left(\frac{\rho_L C_L}{k} \right)^m U^n \quad [2]$$

where

k depends on the hydrodynamics of the flow,

$\frac{dp}{dT}$ is the slope of the vapor pressure temperature curve
at the bulk liquid temperature of interest,

U = a characteristic velocity,

ρ_v and ρ_L are the vapor and liquid densities,

k = the thermal conductivity of the liquid,

L = heat required for vaporization, and

C_s = specific heat of the fluid.

The last two terms are heat transfer factors. The exponents m and n are dependent on the heat transfer process accompanying cavitation. Venturi experiments (3) have established the validity of this relationship. The vapor pressure drop for water at ordinary room temperatures is negligible, the drop for most cryogenic fluids however is significant. If water, however, were superheated to 450°F its local vapor pressure drop would be similar to that of liquid H_2 at -423°F . Lower vapor pressure at the cavity surface means that the local cavitation number of the flow defined as:

$$\sigma_l = \frac{P_{sl} - P_{vl}}{\frac{1}{2}\rho U_l^2} \quad [3]$$

is actually higher than one would calculate based on the bulk fluid vapor pressure. Higher cavitation numbers correspond to lower N_{ss} values and nominally more stable flows. Tests using helical inducers (3,9) have further verified the fact that flow breakdown in liquid H_2 is much delayed over that of water at similar inlet conditions. By the same reasoning, it should be understood that the development of fully "supercavitating" flow such as is required by the design presented later in this report is also delayed to lower cavitation numbers (higher N_{ss} values) than indicated in the data for water tests.

Cavitating cascade performance is presented in terms of the cavitation number while cavitating pump performance is presented using the common parameter of suction specific speed. The two are related in the following manner. Assuming an axial flow machine with no prerotation, the inlet cavitation number will vary in the radial direction. For purposes of comparison, the tip cavitation number will be used since it represents the lowest value of any radial location. The tip cavitation number is defined as:

$$\sigma_t = \frac{H_{static} - H_{vapor}}{w_1^2/2g} \quad [4]$$

where

$$w_1 = \sqrt{U_t^2 + V_f^2}, \quad U_t = \frac{2\pi n}{60} r_t$$

w_1 is the velocity of flow relative to the impeller blade.

Suction specific speed is defined by Equation [1],

where

$$\text{NPSH} = H_{\text{static}} + \frac{V_f^2}{2g} - H_{\text{vapor}} \quad [5]$$

Combining these two relationships and further using the definition of flow coefficient,

$$\phi_o = \frac{V_{f_o}}{U_t} \quad [6]$$

One may obtain the following relationship between σ_T and N_{ss} for an axial flow machine with a 60 percent hub.

$$N_{ss} = \sqrt{\phi_o} \left[\frac{67272}{.41 + \phi_o^2} / \sigma_t + \frac{\phi_o^2}{.41 + \phi_o^2} \right]^{4/5} \quad [7]$$

For other hub-diameter ratios, the constants in the above equation will change. Figure 1 shows the solution of Equation [7] for a variety of tip cavitation numbers and flow coefficients.

Two characteristics of this relationship should be noted. First, there exists an optimum flow coefficient for which a maximum value of N_{ss} can be obtained for each tip cavitation number. Secondly, for each flow coefficient there exists a theoretical maximum possible suction specific speed which occurs when the tip cavitation number (i.e., inlet static pressure) is zero. This maximum possible N_{ss} is strongly dependent on ϕ_0 . Figure 2 shows the influence of flow coefficient in suction specific speed for various hub/diameter ratios assuming a constant tip cavitation number $\sigma_t = 0.010$.

3.0 BACKGROUND

In the previous work of Reference (12), it was decided to use a supercavitating first stage and to base the head rise produced by the first stage on the maximum allowable value within the limits of certain stability requirements. A generalized theory for the prediction of instabilities caused by self-induced circumferential distortion or rotating stall (15) was used to determine this maximum stable head rise. The application of this theory required a knowledge of the performance of supercavitating cascades under various inflow conditions.

It was concluded by Auslaender (21) that an isolated foil which has a constant pressure camber distribution should have nearly optimum performance for supercavitating propellers and pumps. It was therefore decided to design the first stage of

the inducer pump to obtain all lift from constant pressure camber. The development of a two-dimensional cascade theory for sections with constant pressure camber and finite cavity length was thus essential.

The performance of supercavitating cascades with constant pressure cambered blades and finite cavity lengths was studied theoretically using potential theory for cavity flows and a suitable model for finite cavity length. The results were published in (22) and (23).

The procedure used in the design of the supercavitating first stage was the familiar free-vortex, blade element theory described in References (24) and (25). This design method allows the design to be based on the performance of two-dimensional supercavitating cascades. The design equations are presented in Reference (12).

The design method for the second stage of the tandem row inducer was based on the theory for axial flow pump design presented in Reference (26). This method accounts for induced interference effects at an impeller blade as influenced by the other blades and the total downstream vorticity along the pump centerline. Optimization of the cavitation performance of the second stage is also accounted for in the procedure.

A design for a two stage inducer utilizing constant pressure cambered supercavitating sections in the first stage and meeting the design requirements while maintaining stable flow required

that 15 percent of the total head be generated by stage 1 and 85 percent by stage 2. It became apparent from the test program of Reference (12) that the design goal of $N_{ss} = 30,000$ was unlikely to be reached using cascades of constant pressure cambered foils. One characteristic of such cascades is that as solidity is increased, the camber of the foil is reduced and finally approaches a flat plate. This is detrimental to the stability of the flow since flat plate profiles create a higher drag for the same lift than cambered profiles. The flat plate must rely entirely on angle of attack for lift generation.

To further improve the capability for tandem inducer design, a theoretical study of higher term cambered supercavitating cascades was conducted. The types of foils considered in this study were the circular arc and two, three, and five term cambered sections (27). The results for fully supercavitating foils and partially cavitating foils were published in (28,29,30,31). As an extension and refinement of the second stage design procedure (26), an expanded theoretical study of a radial line vortex in annular space (32) was completed for various hub/diameter ratios and smaller axial and tangential spacings (33). Improved methods for calculating interference streamlines and coefficients were developed. And finally, tentative new first and second stage inducer designs were conducted.

A number of five-term cambered supercavitating first stage designs were considered using the theoretical cascade results and the approach of free vortex design and blade element theory. The overall inducer requirements were taken to be the same as for the constant pressure cambered case previously described.

Among the five term cambered cases considered were two and three bladed designs using first order and approximate second order (31) results having:

- (a) specified linear C_L variation with radius
- (b) constant chord length with radius
- (c) constant solidity with radius (radial leading and trailing edges)
- (d) specified linear chord length variation with radius

The two bladed, second order, constant chord length design was chosen. Lining up the trailing edges in a radial direction results in a swept leading edge. The swept leading edge has been shown (4) to have certain advantages with regard to stability and in addition has definite structural advantages. The swept or spiral leading edge has also been used in a number of operational rocket engine inducers including the J-2 and F-1 engines for the Saturn V launch vehicle. The design, assigning 15 percent of the total head rise to the first stage was shown to be marginally stable at the design point and mid-radius using the criteria of (15).

Using the calculated results for the radial vortex filament in an annular space (33), numerous second (subcavitating) stage designs were considered using the design technique of (26). The design chosen utilized 4 blades and a 0.70 hub/diameter ratio. Six vortices per blade were used in the design procedure and the NACA 65 series camber and 16-009 thickness function were used to arrive at the final blade profiles.

The two bladed, five-term cambered first stage was manufactured and tested. A significant improvement was achieved over the performance of the constant pressure cambered first stage previously investigated. The design head coefficient (15 percent of .25) and suction specific speed (30,000) were both achieved but at a flow coefficient of 80 percent of the design value.

A first stage model having the same blade profiles but with three blades was constructed in the belief that the higher solidity blades might improve overall head generation and thus delay breakdown to a higher N_{ss} value at a higher flow coefficient. The blades were also reduced in pitch by 1° to increase the flow coefficient operating range. The resulting three bladed five-term cambered first stage was manufactured and tested in the pump test loop. The addition of the third blade greatly increased the head generation at low N_{ss} values, but reduced the breakdown N_{ss} value at all flow coefficients.

Analysis of the cavity length data for both models indicated that, provided the flow coefficient was below a certain critical value, the region of severe oscillations corresponded to that operating condition where the cavity collapsing from one blade extends back to or slightly beyond the leading edge of the adjacent blade. The oscillation of the flow in the unstable region appears to be of the limit cycle type, but the exact mechanism is uncertain. From the analysis, however, it may be concluded that the oscillations are probably due to the interaction of the cavities with adjacent blades at critical cavity lengths and thicknesses. Because of the complex flow at the entrance to the gap formed by the adjacent blade, the cavity length-head relationship may be inherently unstable leading to cavity length oscillation between fixed boundaries.

In the large "stable" region of operation, an analysis of the magnitude and frequency of oscillations in the 0-100 cps range indicated that peaks occur in the vicinity of 20 cps and 85 cps. Neither pressure peak exceeded 10 percent of the head generated by the first stage and for N_{ss} values of 22,000 or less neither exceeded 5 percent. Correlation with l/c indicated a minimum at about $l/c = 1.40$.

No tandem tests were conducted for the five-term cambered inducers of (13) and no second stage model was constructed. It was concluded, however, that the type of inducer investigated might well be an alternative to the simple helical types presently

used. This approach would appear to be even more attractive as future performance requirements become more severe with regard to higher speeds, lower flow coefficients, and higher total head generation requirements.

The present work presents the design and testing of a tandem inducer configuration based on the theoretical and experimental background referenced and intended to further demonstrate the feasibility of the tandem inducer concept having supercavitating first stages. Due to limited funding, the second stage design was required to be a helix rather than the recommended cambered airfoil design. An unfortunate choice of helix angle resulted in a second stage with considerably lower head rise than desired. The second stage and tandem test results later reported are therefore of limited interest. The critical first stage, however, was built and tested as recommended.

4.0 INDUCER DESIGN

General Considerations

Overall design requirements for the tandem inducer were chosen as those used for the program of (13). This decision was based partly on comparison of the design criteria to the J-2 LOX inducer which is presently considered to be the prime example of a prototype counterpart. Table 1 reviews these design conditions. The choice of a 60 percent hub ratio was based on compatibility with previous models. It should be noted that the

TABLE 1
Design Parameters Compared to
J-2 LOX* Inducer

Parameter	J-2 LOX*	1st Stage	2nd Stage
Diameter, inches	6.75	7.0"	7.0"
Hub ratio, η_H	0.204	0.60	0.70
Number of blades	3	2	4
Rotational speed, rpm	8800	4000	4000
Inlet flow coef., $\phi_o = V_f/U_t$	0.1006	0.100	-
Head coef., $\psi = gH/U_t^2$	0.080	0.0375	0.2125
Suction Specific Speed, $N_{ss} = \frac{n\sqrt{Q}}{NPSH^{1/4}}$	32,500	30,000	-
Corrected N_{ss} , $N'_{ss} = N_{ss}/\sqrt{1-\eta^2_H}$	33,400	37,400	-

*Equivalent inlet conditions in water not LOX, at a selected operating point for $\phi_o \approx 0.10$.

suction specific speed of the first stage of the tandem inducer has a slightly lower value of suction specific speed than the J-2 LOX inducer, but actually has a higher value of "corrected" suction specific speed defined as

$$N'_{ss} = N_{ss} / \sqrt{1 - \eta_H^2}$$

where η_H is the ratio of hub to tip radius. The corrected suction specific speed is a more accurate reflection of the severity of the design condition for the impeller.

First Stage Design

The five term cambered blade profile for the first stage was retained with a slight modification. The experience of (13) indicated a considerable amount of face cavitation during a portion of the operating range. The "modified" five term shape flattens out the convex curvature of the forward half of the blade slightly. This leads to a more wedge-like leading edge intended to improve face cavitation. The constant chord concept leading to a swept leading edge when the trailing edges are radial was retained and the design calculations were conducted at three radii with intermediate sections faired. The blunt trailing edge typical of supercavitating sections was also retained but was slimmed somewhat to improve off-design operation with no significant sacrifice in structural strength. In order to reduce gap cavitation, the recommendations of (34) with regard to tip clearance and corner radius on the pressure side edge were used.

The general design procedure followed was the same as presented in (12,35). In the case of the higher term cambered (or more properly, arbitrarily cambered) case, the theory of Hsu (28) was used to generate cascade characteristics. The detailed design procedure developed to utilize these results is outlined by the following:

- (a) Select the desired flow coefficient, φ_o ; head coefficient, Ψ ; maximum suction specific speed, N_{ss} ; tip diameter, D_t ; hub ratio, D_h/D_t ; rpm; and head distribution between first and second stages.
- (b) Choose the form of radial head variation (again free vortex or constant head with radius has been used) and calculate the swirl (ΔV_u) variation from the required Euler head, $\Delta V_u = \frac{gH}{U}$.
- (c) Construct the inlet and outlet velocity triangles and calculate the local cavitation number variation, σ_i .
- (d) Calculate the required value of $\frac{C_L}{\sigma} \frac{c}{d}$ from

$$\frac{C_L}{\sigma} \frac{c}{d} = \frac{2gH}{\sigma U^2} \sin \beta_1. \quad (\text{Ref. 12})$$
- (e) Select the desired camber type (circular arc, 2-term, 3-term or 5-term cambered) and an arbitrary camber coefficient, k .

- (f) From a plot of cavitation number, σ , versus solidity, c/d , for various angles of attack, α_o , (for the stagger angle, camber type, and camber coefficient selected) assume a value of c/d and get the corresponding α_o for the local cavitation number.
- (g) From the corresponding $\frac{C_L}{\sigma} \frac{c}{d}$ versus c/d plot (for the long l/c range as discussed in Reference 35) using the value of α_o selected find the value of c/d which yields the required $\frac{C_L}{\sigma} \frac{c}{d}$. If this c/d doesn't agree with the one selected in step (f), return to step (f) and repeat. Continue to iterate until the values agree.
- (h) Using the value of c/d and σ obtain the value of C_L from $\frac{C_L}{\sigma} \frac{c}{d}$. As a check compare this to the value on the plot of C_L versus c/d for the required α_o .
- (i) Repeat steps (b) - (h) for a range of camber coefficients and radii of interest. Then using the results, construct the following plots for each radius:

C_L versus k

c/d versus k

and α_o versus k

for constant σ , $\frac{C_L}{\sigma} \frac{c}{d}$, and β .

These plots then allow flexibility in the choice of camber coefficient for a given design requirement.

- (j) Select an arbitrary design parameter variation which is desired to be characteristic of the design. For example, one might choose:

linear C_L variation with radius
constant chord length with radius
constant solidity
linear chord length variation
or some other variation as desired.

- (k) After selection of the parameter variation in step (j), use the C_L , c/d , and α_o versus k plots to select the final cascades required for the design.
- (l) From the theory (28), calculate the exact cascades required and check against the interpolated values.

The final step of the design which was formerly to check the stability of the design against the Yeh (15) stability criterion has been deleted since that parameter failed to correlate with the onset of instabilities in the test programs of (12) and (13).

During the previous tests of five-term cambered supercavitating inducers (13) it was concluded that the theory for supercavitating cascades of cambered foils (28) agreed rather well with test data provided that the local flow conditions were nearly two-dimensional and that fully supercavitating conditions actually existed. This was most nearly the case at mid radius. It was also concluded that the complex three dimensional flow field which is present in the actual inducer requires that corrections to account for real fluid and three dimensional effects be included in the design procedure. The design procedure of (13) was judged to be an adequate first step which should be built upon.

In the present design, the experience and recommendations of (13) have been utilized and a significantly improved design has resulted. As was previously noted, the second order, five-term cambered, constant chord design with a 60 percent hub ratio has been retained for stage 1 and the five term cambered profile has been slightly modified to flatten out the convex curvature on the forward half of the blade. This leads to a more wedge-like leading edge and should improve resistance to face cavitation observed during previous tests (13).

In addition, a number of other basic steps have been taken to empirically modify and improve the design procedure. These relate to the problems of (a) non-uniform head generation with radius, (b) poorer than desired suction performance and (c) lower than desired optimum flow coefficient.

With regard to the non-uniform head generation, it can be observed from Figure 41 of Reference (13) that for both the two-bladed and three-bladed models at high N_{ss} values, more head was generated at the tip radius than at the hub, even though the design nominally specified uniform head generation. This has at least three undesirable effects on performance. First, the inflow to the second stage is non-uniform with radius, a condition which may be partially alleviated with greater distance downstream from the first stage. Second, with higher head generation at the tip, the problems of tip and gap cavitation are aggravated. This is due to the higher resultant differential pressure between the suction (back) and pressure (face) surfaces. Higher differential pressure results in a greater driving force through the gap and, therefore, greater gap flow and cavitation. It also results in a higher vorticity at the tip, increasing tip cavitation. In marine propeller applications, tip vortex cavitation is a major source of propeller generated noise and tip unloading (lowering of tip lift coefficient) is commonly used to alleviate the problem. The third complication due to non-uniform head generation is a structural side effect. With higher tip loading, the root bending stress is increased over that with uniform radial loading for the same overall head generation.

The present design attempts to compensate for this non-uniform head generation due to three dimensional effects. Based on the results of (13), the present design head at the tip and hub are respectively reduced and increased by about 20 percent. This was done empirically with the expectation that three dimensional effects will result in a nearly uniform head generation with radius.

The second problem of poorer than desired suction performance has been accounted for by designing for an even lower NPSH or higher N_{ss} . Both the two and three bladed designs of (13) achieved design head coefficient (.0375) and design flow coefficient (.10) values at approximately $N_{ss} = 25,000$ rather than 30,000. Table 2 presents the design values of local cavitation number at each of the three radii compared to achieved values at $\psi = .0375$, $\varphi_o = .100$.

In terms of NPSH, the Reference (13) design value was 8.81 feet while the achieved value was 11.25 feet. The value used for the present design was therefore calculated by reducing the inlet static pressure to 56 percent of the desired value. The resultant design NPSH is 7.43 feet and the resultant local cavitation numbers are shown in Table 2.

Since in Reference (13), a lower than desired value of optimum flow coefficient, φ_o , resulted in best performance (0.08 as compared to design value of 0.10); the angle of attack has been empirically increased slightly (15 percent) at all radii to favor higher φ_o performance.

TABLE 2

Reference (13) and Present Local Cavitation
Numbers at Design Flow and Head Coefficients

	<u>TIP</u>	<u>MID</u>	<u>HUB</u>
Reference (13) Design Cavitation No.	0.0132	0.0203	0.0352
Reference (13) Achieved Cavitation No.	0.0234	0.0361	0.0626
Reference (13) Ratio of Design to Achieved	0.56	0.56	0.56
Present Design Cavitation No.	0.0074	0.0114	0.0197

Each of the above discussed design modifications is of a strictly empirical nature based on the previous experimental work. They were each incorporated knowing that the resultant design would be of a "one-shot" nature with no chance for systematic empirical deviation from the originally selected design configuration. All of the design modifications were believed likely to improve the first stage performance from both a hydraulic and suction performance viewpoint.

Due to the above detailed empirical design modifications, one obtains two sets of design parameters. The first set consists of the two-dimensional, ideal fluid parameters chosen for design calculation. The second set consists of the actual three-dimensional, real fluid performance expected due to the design parameters chosen. Both sets are detailed in Table 3. All

TABLE 3

Stage 1 Detailed Design Summary, $\phi_0 = 0.10$, 4000 rpm

(All velocities in f.p.s. angles in degrees and lengths in inches.)

	2-D Design Values Used			3-D Performance Expected		
	TIP	MID	HUB	TIP	MID	HUB
Head coefficient, ψ	0.0300	0.0375	0.0450	0.0375	0.0375	0.0375
Local cavitation no., σ	0.0074	0.0114	0.0197	0.0132	0.0203	0.0352
Peripheral speed, U_p	122.2	97.8	73.4	122.2	97.8	73.4
Axial velocity, V_{f_1}	19.12	19.12	19.12	19.12	19.12	19.12
Velocity relative to blade, w_1	123.6	99.6	75.85	123.6	99.6	75.85
Swirl velocity, AV_u	3.66	5.72	9.18	4.58	5.72	7.65
Radius, R	3.50	2.80	2.10	3.50	2.80	2.10
Chord length, C	5.41	5.41	5.41	5.41	5.41	5.41
Solidity, C/D	0.492	0.615	0.820	0.492	0.615	0.820
Head parameter, $\frac{C_L C}{\sigma D}$	8.00	10.01	12.26	5.61	5.66	5.71
Camber coefficient, K	0.137	0.217	0.320	0.137	0.217	0.320
Lift coefficient, C_L	0.120	0.185	0.295	0.151	0.187	0.245
Local head generation	13.90	17.40	20.90	17.40	17.40	17.40
Relative inlet angle, β_1	81° 07'	78° 56'	75° 22'	81° 07'	78° 56'	75° 22'
Relative mean angle, β_m	80° 59'	78° 36'	74° 27'	80° 55'	78° 36'	74° 38'
Relative outlet angle, β_2	80° 50'	78° 16'	73° 24'	80° 46'	78° 16'	73° 48'
Chord line angle of attack	3.63°	4.50°	6.44°	3.63°	4.50°	6.44°
Nominal ref. line angle of attack*	4.95°	6.90°	9.54°	4.95°	6.90°	9.54°
Chord line blade angle**	12.46°	15.57°	21.07°	12.46°	15.57°	21.07°
Ratio of l.3. pressure surface angle of attack to blade angle	0.397	0.443	0.453	0.397	0.443	0.453

*Also represents leading edge pressure surface angle of attack.

**Equivalent to blade angle (90°-stagger) as defined by Reference (36).

performance parameters presented are for operation of the inducer at 4000 rpm. As will be noted later, most tests were conducted at lower rpm.

Figure 3 shows the full scale blade sections chosen for the first stage at the tip, mid and hub radii. Figure 4 shows the completed impeller design as it appeared in three dimensions wrapped about the 60 percent cylindrical hub.

Figure 5 shows a photograph of the completed five-term cambered supercavitating first stage model which was manufactured by HYDRONAUTICS, Incorporated from 7075-T651 aluminum and black anodized. The blades were individually machined from patterns (Figure 6) and fit into a separate hub. Figure 7 compares the leading and trailing edge profiles of the first stage to those of the Saturn V engine inducers.

Transition Design

References (37) and (38) present the results of a study of conduit contractions. It was shown that a contraction consisting of matched cubic arcs (i.e., arcs of the form $y = x^3$) is preferable to either elliptical or circular arcs with regard to resistance to cavitation or separation. The study was conducted experimentally using an electrical analog to the fluid flow problem. The effect of contraction geometry on the development of adverse pressure gradient and local pressure coefficient variation resulted in a parametric graph yielding the maximum allowable

downstream location of the inflection point (juncture of the two cubic arcs) as a function of upstream and downstream diameter and contraction length.

By analogy to the conduit contraction, this method was used to design the transition section between the 60 percent hub of the first stage and the 70 percent hub of the second stage. Since the outer radius of the flow annulus remains a constant and the inner radius changes, the problem is much like an "inside-out" conduit contraction where the outer wall changes radius while the inner radius remains constant (equal to zero in the most common case of a circular pipe).

In the present case, the length of the transition was fixed by the closest desired spacing between inducer stages. The results of (13) and (39) indicate that a spacing of between 0.5 and 1.5 inches for inducers having diameters of 5.5 to 7.0 inches is probably near optimum. The length of 1.50 inches was therefore chosen in which to make the transition from a 2.10 inch (60 percent) radius cylindrical hub to a 2.45 inch (70 percent) radius cylindrical hub.

Using the width of the annular space as analogous to the diameter of the equivalent pipe, it was determined that the inflection point could be located at 25 percent of the transition length. The equations of two cubic arcs tangent to the cylindrical hub surfaces and tangent to each other at the inflection

point were then calculated and used to generate the required transition offsets. Figure 8 shows the transition shape at times full scale. Figure 9 shows the completed transition section which was manufactured by HYDRONAUTICS of aluminum and black anodized.

Second Stage Design

Simplification of the problem of finding the three-dimensional potential flow field for a finite number of blades of constant circulation in an axial turbomachine to the determination of the three-dimensional field due to a single radial vortex filament of uniform strength in a cylindrical annulus has been made by Tyson (32). For more than one blade, the solution may be found by superposition of the single filament fields.

The calculation of (32) were repeated by HYDRONAUTICS (33) and expanded to cover more hub-ratios and closer radial station spacing.

The pump impeller technique of Bowerman (26) utilizes the results of the three dimensional velocity field calculation. The design method consists of representing each impeller blade by a number of radial line vortices. One blade is removed from the impeller and the interference streamline due to all the other blades and the total downstream vorticity is calculated. The camber and thickness distributions are then superimposed on the interference streamline, resulting in the final impeller design. The technique allows the design of an impeller without

the use of experimental or theoretical cascade data. This is especially helpful in the case of inducers where high solidity and high stagger angles are required, since cascade performance in this range is not known. The lack of knowledge of cascade performance in this range is a major factor in the adoption of a simple, helical blade to inducer applications.

In Reference (12), the second stage of a tandem-row inducer was designed using the Bowerman design technique. Tests of this stage indicated the need for empirical modifications to improve performance. The results given by Tyson (32), however, were used in this design. The later calculations by HYDRONAUTICS (33) disagreed substantially with the results of (32) at all but the mid-radius. The complex velocity potential which must be determined for the three dimensional solution is given by:

$$\Phi = \pm \frac{1}{4\pi} \left(\theta + 4 \sum_{m=1}^{\infty} \frac{\sin m\theta}{m} \sum_{n=1}^{\infty} \frac{\beta_{nm}}{\gamma_{nm}} Z_m \left(\frac{\mu_{nm} \eta}{\eta_H} \right) e^{\mp \frac{\mu_{nm} \xi}{\eta_H}} \right)$$

where the sign difference refers to the regions upstream and downstream of the filament location, and

Φ = dimensionless velocity potential Φ/Γ ,

β_{nm} = constant,

γ_{nm} = constant,

J_m = Bessel function of the first kind,

Y_m = Bessel function of the second kind,

B_{nm} = constant,

$Z_m = J_m + B_{nm} Y_m$,

μ_{nm} = dimensionless Eigenvalue $\lambda_{nm} a$,

η_H = hub ratio, a/b ,

η = dimensionless radial coordinate, r/b , and

ξ = dimensionless axial coordinate, x/b .

The dimensionless velocity components in the axial, radial and tangential directions may then be determined from:

$$C_\xi = \frac{\partial \phi}{\partial \xi}$$

$$C_\eta = \frac{\partial \phi}{\partial \eta} \quad , \quad \text{and}$$

$$C_\theta = \frac{\partial \phi}{\partial \theta}$$

To superpose the velocity fields due to a number of filaments:

$$V = v \left(\theta + \frac{2\pi}{N} \right) + v \left(\theta + 2 \frac{2\pi}{N} \right) + \dots + v \left(\theta + N \frac{2\pi}{N} \right)$$

where

N = the number of filaments,

V = the resultant tangential, radial, or axial velocity, and

v = the tangential, radial, or axial velocity component due to a single filament.

A substantial simplification to the problem can be made if a two-dimensional approximation is made. The resultant tangential and axial velocity components may be shown to be (35):

$$C_{\theta} = - \frac{1}{4\pi\eta} \frac{\sinh(\xi/\eta)}{\cosh \xi/\eta - \cos \theta}$$

$$C_{\xi} = \frac{1}{4\pi\eta} \frac{\sin \theta}{\cosh \xi/\eta - \cos \theta}$$

Figure 10 shows the variation of $C_{\theta_{total}}$ with axial location, ξ , as obtained using the three-dimensional and two-dimensional results for an interference streamline calculation using the following conditions:

Impeller diameter = 7.0"

Diameter under consideration, $\eta = 1.00$

Hub/diameter ratio, $\eta_H = 0.70$

Lift parameter, $C_L(C/D) = 0.493$

Solidity, $C/D = 1.795$

Chord, $c = 9.87"$

Axial extent ratio, $\xi_t = 0.641$
Diffusion factor = 0.275
Number of blades = 4
Vortex filaments/blade = 6
Design flow coefficient = 0.10
2nd stage design head coefficient = .2125
rpm of impeller = 4000
1st stage design head coefficient = .0375

While there are discernable differences, the calculation indicates that, at least for hub/diameter ratios of 0.70 or greater, there is not enough difference between the results to justify the calculation of the more complicated three-dimensional values.

During the tests of the second stage inducer of (12) neither the total head nor the axial velocity remained constant along the radius as assumed in the design. A contributing factor causing this difficulty was flow separation along the hub section and resulting flow "pile up" at the tip sections. The diffusion factor has been shown to correlate well with limiting blade loading or separation in axial flow compressor blades.

$$D = \left(1 - \frac{w_2}{w_1} \right) + \frac{\Delta V_u}{2(c/d)w_1}$$

Correlation with NACA compressor data shows that to avoid separation this factor should be less than 0.60. The Reference (12) second stage design called for diffusion factors at the tip radius, mid radius, and hub radius of 0.259, 0.362, and 0.701 respectively. The diffusion factor at the hub was too large because of the high head coefficient and low peripheral speed. It could have been reduced by increasing the hub diameter ratio, but the necessary annular velocity distributions for the Bowerman method were only available for a 0.60 hub at the time.

For the new second stage design, a hub ratio of 0.70 was chosen. The design technique was that of Bowerman (26) with slight modifications. Specifically, the Bowerman technique results in a prescribed variation of chord with radius as a result of the optimization of cavitation performance.

In the present design, the variation of chord with radius was arbitrarily prescribed. This is a minor consideration for the high solidity blades and large hub ratio of the present design for which Bowerman's cavitation optimization has little effect. The chord variation chosen was such that the blades had 180° wrap at the hub and a 60° leading edge sweep. The parameters of this design are tabulated in Table 4. The overall design utilized the following:

Number of blades - 4

Vortices per blade in Bowerman technique - 6

TABLE 4
Summary of Stage 2 - Four Bladed Design

Quantity	Tip Radius (3.5")	Mid Radius (2.975")	Hub Radius (2.45")
Head coefficient, ψ	0.2125	0.2125	0.2125
Peripheral speed	122.2 fps	103.8	85.5
Axial flow velocity	24.0 fps	24.0	24.0
V_u , inlet	4.57 fps	5.38	6.53
ΔV_u	26.0 fps	30.65	37.20
C_l c/d	.493	.710	1.114
C	9.87 inches	8.95	8.26
C/D	1.795	1.92	2.15
C_d	.275	.370	.519
ξ_t , axial extent	.641	.709	.849
Diffusion factor	.275	.385	.511
θ , tangential extent	157.3°	165.6°	180°
β_1	78° 15'	76° 18'	73° 28'
β_2	76° 51'	73° 54'	68° 56'
β_m	75° 02'	70° 29'	61° 17'

Camber type - NACA "65"

Thickness distribution - NACA 16-009 function

Thickness - tip 1.5%, mid 2.5%, hub 4.5%

Hub ratio - 0.70

The tangential component of velocity V_u due to all of the other blades is non-dimensionalized as follows:

$$C_\theta = \frac{V_u r_t}{\Gamma}$$

The value of C_θ in (12) and (26) was found to vary almost linearly with non-dimensional axial distance $\xi = z/r_t$. Thus,

$$C_\theta \approx k_0 + k_1 \frac{\xi}{\xi_t}$$

where ξ_t is the value of ξ at the trailing edge of the foil.

In the present design, a slightly closer fit to the variation of C_θ with ξ was found to be

$$C_\theta = k_0 + k_1 \frac{\xi}{\xi_t} + k_2 \sin \left(2\pi \frac{\xi}{\xi_t} \right)$$

The streamline equation, which defines the streamline at each radius about which the isolated cambered blade shape must be placed is thus found to be

$$\theta = \frac{\xi}{\varphi} \left(1 - \frac{\lambda}{\eta} \right) - \frac{n\Gamma_b}{\varphi r_t^2 \omega \eta} \left[k_0 \xi + \frac{k_1}{2} \frac{\xi^2}{\xi_t} - \frac{k_2}{2\pi} \xi_t \cos \left(2\pi \frac{\xi}{\xi_t} \right) \right]$$

where:

$$\varphi = \frac{V_a}{U_t} = \frac{V_a}{\omega r_t}$$

$$\lambda = \frac{V_{\theta_1}}{U_t} = \frac{V_a}{\omega r_t}$$

n = number of blades

V_a = axial velocity

V_{θ_1} = inlet tangential velocity

$\eta = r/r_t$

$\xi = z/r_t$

Γ_b = circulation per blade

ω = rotational speed

k_0 , k_1 and k_2 are as previously defined and based on total circulation for all blades.

The values of k_0 , k_1 and k_2 for three radii are presented below:

$\frac{r}{r_t}$	k_o	k_1	k_2	ξ_t
0.70	.0199	.1875	.010	.849
0.85	.0217	.1441	.010	.709
1.00	.0214	.1162	.008	.641

A camber line of the NACA 65 series was chosen so that the pressure distribution would be such that possible blade cavitation would be minimized (26). A thickness distribution of the NACA 16 series was used. These distributions along with the above design procedure determine the final coordinates of the foil.

Figure 11 shows the final recommended blade profiles for the second stage and Figure 12 presents a view of the three dimensional impeller as it appears when the sections are wrapped around the required 0.70 hub.

As was previously mentioned, the level of funding available required that the second stage design be compromised from the recommended geometry to a somewhat simpler shape. It was felt that a simpler helical shape could be utilized to demonstrate the behavior of the improved first stage design when operated in tandem with a second, but non-optimum second stage.

The second stage design chosen used four helical blades having 180° of wrap at the hub and radial leading and trailing edge profiles. Figure 13 shows two views of the second stage

impeller design. Only one of the four identical blades spaced at 90 degrees is shown. The pressure surface of the second stage blade design is a constant pitch helix with a nominal pitch angle of 76.21 degrees at the tip radius measured from the axis of rotation of the impeller. With a constant lead, this produces a helix with nominally a 70.66 degree pitch angle at the hub radius.

The back surface of the blade was generated by adding a thickness distribution to the helical face. One half of the NACA Series 16 basic thickness distribution was used. The thickness at each chordwise hub station is twice the thickness of the corresponding tip chordwise station. The chord lengths at the tip and hub are respectively 11.32 inches and 8.12 inches. Corresponding thickness/chord ratios are 1.10 percent and 3.08 percent. Equivalent cascade solidities for the inducer second stage were 0.820, 0.615, and 0.492 at the hub, mid, and tip radii respectively.

The choice of blade angle used for the helical second stage was unfortunate. The pitch used was near the nose-tail line pitch of the detailed airfoil design previously presented. This design relied heavily on foil camber to generate head. Since the helical blade has no camber, the design head generation of the second stage shifted toward much lower flow coefficient than desired. This will become apparent in the later data presentation.

Based on the recommendations of (34) a radius of 0.040 inches is used on the pressure side tip of the blades for both stages 1 and 2. This is equal to twice the tip clearance gap and was chosen to reduce the occurrence of the tip gap cavitation as compared to the sharp (90 degree) corners.

The second stage impeller was manufactured by a subcontractor with integral blades and hub being machined from a single piece of 6061-T6 Aluminum. Figure 14 shows a photograph of the black anodized model.

Figure 15 shows the complete two stage inducer model with the transition section between stages increasing the hub diameter to tip diameter ratio from 0.60 to 0.70. The tip diameter of the first and second stages is a constant 7.0 inches.

5.0 TEST FACILITY AND PROCEDURE

The experimental program was conducted in the HYDRONAUTICS, Incorporated pump test loop. Figure 16 shows an overall view of the pump loop instrumentation, control and data acquisition systems. In the foreground, the control panel contains starting and stopping controls for the main pump loop motor, filter pump, vacuum pump, heat exchanger, and bearing lubrication and pressurization pump. In addition, the running speed control, a dial rpm indicator, and solenoid controlled valve switches are on this panel. Directly above the control panel is the pump loop test section with three direction-velocity probes installed. Flow through the pump loop is from right to left. Manifolds and valves visible above the test section and on the board to the right connect the pressure transducers to digital readouts. To the far right is the HYDRONAUTICS, Incorporated data acquisition system from which digital outputs are recorded.

Figure 17 shows a closer view of the test section area. A single impeller can be seen through the plexiglas test section which is square on the outside and cylindrical on the inside. The three United Sensor velocity probes on the top of the test section are aligned for flow direction with a Pace transducer mounted on the board above. On the board to the right, three additional Pace transducers of various ranges are used for individual pressure readings. All pressures are referenced to the Uehling mercury column absolute pressure gage on the far right side of the panel. On the reverse side of this panel is mounted the General Radio wave analyzer used to measure fluctuating pressure spectra in the 0-100 cps range from the output of an Atlantic Research transducer.

The plexiglas test section of the loop is 22 inches long with an internal diameter of 7 inches. Plexiglas was used to make observations of the onset and extent of cavitation possible.

The entire pump loop can be pressurized to eliminate cavitation or the pressure can be reduced to low absolute values to simulate low cavitation numbers. Thus, pumps can be tested at suction specific speeds higher than 30,000. A continuously variable speed 150 hp drive provides a shaft speed up to 5000 rpm. A torque and thrust dynamometer located on the shaft downstream of the test section enables these quantities to be measured. A specially designed valve downstream of the test section allows flow regulation. A heat exchanger allows the water temperature

to be kept steady even though considerable heat may be generated by the dissipation of energy in the water.

United Sensor velocity probes of the type shown in Figure 18 are inserted through the test section wall for radial surveys of pressures, velocities and flow angularity. The probes can be located at several points in the test section. Arrangements are provided to effectively bleed air bubbles from the tubing. This can be a major source of error especially at low absolute pressures. The shaft rpm is approximately set by an rpm meter and accurately measured by means of a calibrated strobe light, which is also essential for observation of the type and extent of cavitation occurring on the blades.

The test procedure adopted for all impellers was the same as that used for cavitation tests on a conventional pump. The flow coefficient is held constant and the net positive suction head (NPSH) of the pump lowered until the total head decreased rapidly due to cavitation. The pressure upstream of the impeller is first reduced to the required value. The valve downstream of the pump is then regulated until the required flow coefficient is obtained. Measurements of the static and total pressures and flow angularity are made at 5 or 6 radial positions upstream and downstream of the impeller. These data are processed by an IBM 1130 computer which integrates the pressures and velocities and calculates the appropriate performance parameters and coefficients.

Unsteady components of the flow through the inducers were recorded by measuring the unsteady or fluctuating pressures in the range of 0-100 Hz. An Atlantic Research piezo-electric transducer calibrated to 770 mv/psi was used in conjunction with a General Radio wave analyzer and an impedance matching unit. The wave analyzer bandwidth was 3 Hz and measurements were taken at no more than 5 Hz intervals from 0-100.

6.0 TEST RESULTS AND DISCUSSION

Figure 19 shows the influence of suction specific speed on first stage head coefficient at a number of flow coefficients. The gradual reduction of head generation as suction specific speed increases (NPSH decreases) is typical of the performance of supercavitating or fully cavitating impellers. Fully wetted impellers by contrast have a rather constant ψ - N_{ss} relationship until some critical region in which ψ falls precipitously with further decrease in NPSH. It will be shown later that the tandem configuration modifies this overall relationship toward that of the fully wetted impeller.

A suction specific speed of nearly 32,800 was achieved at a flow coefficient of 0.0698. At 30,000, the design suction specific speed, the design head coefficient for the first stage, .0375, was achieved at a flow coefficient of 0.060. This is only 60% of the desired 0.10 value, a result similar to the two stage five term combined impeller of Reference (13) in which the design point was achieved at 80% of the desired flow coefficient.

Figure 20 shows the head coefficient-flow coefficient relationship for the first stage at various suction specific speeds. It is notable that no regions of severe self-induced oscillations were observed over the entire test range. At the conclusion of the tandem tests, a number of isolated first stage tests were conducted in which more severe head fluctuations were noted for similar conditions than in the tandem tests. This will be discussed in more detail later. The ψ - ϕ plot also indicates a rather flat head-discharge relationship with suction specific speed a much stronger influence on head generation than flow coefficient. It may also be concluded from this plot that the design head and flow coefficient values could be obtained with the first stage impeller at a suction specific speed of about 21,000.

Figures 21 and 22 indicate performance of the second (helical) stage when operated in tandem with the first (supercavitating) stage. It should be noted at this point that the first stage did not actually operate fully supercavitating over most of the test range and, in fact, was designed to operate supercavitating only at the design point. Figure 21 shows the influence of first stage suction specific speed on second stage head generation. The apparent strong influence of N_{ss} on the second stage is really more a result of the strong relationship between first stage head generation and N_{ss} than a direct cavitation related performance characteristic of the second stage.

As the suction specific speed is increased, first stage head generation drops off (see Figure 19) and therefore less turning of the flow (lower ΔV_u) occurs. This results in a higher angle of attack on the second stage impeller blades and, therefore, higher second stage head generation. By comparing Figures 19 and 21 this inverse relationship becomes apparent.

Figure 22 shows the head coefficient-flow coefficient relationship for the second stage impeller when operated in tandem. As a result of the pitch angle chosen for the helical inducer at near the mean pitch angle of the more desirable second stage having cambered blades, the second stage generated considerably less head than the original cambered design and operated at lower flow coefficient. The second stage performance was adequate for the purpose of demonstrating tandem operation, however, and in light of the first stage performance favoring lower than design flow coefficients the impellers were not badly matched for low ϕ operation. From Figure 22 it is apparent that the slope of the ψ - ϕ relationship is much steeper for the second stage than the first stage and that the first stage suction specific speed (more correctly first stage head generation) has a profound effect on second stage head generation. The first stage achieved design head coefficient (.0375) and design suction specific speed (30,000) at a flow coefficient of 0.060. If this operating point is placed on Figure 22 we see that the second stage generated a head coefficient of 0.175 for this condition.

Figures 23 and 24 indicate the overall performance of the tandem inducer. Figure 23 shows the influence of suction specific speed on head generation at various flow coefficients. The flattening out of the effect of suction specific speed is apparent when this plot is compared to Figures 19 and 21 for each stage. Figure 24 showing the ψ - ϕ relationship is more dramatic in illustrating this point. All data from suction specific speeds of 5,000 through 25,000 lie in the narrow shaded band. Higher suction specific speeds at lower flow coefficients do tend to indicate a fall-off in overall head generation.

Figure 25 compares the first stage suction performance of the present inducer to typical results for two and three bladed inducers having constant-pressure camber and five-term camber from References (12) and (13). It is apparent from this plot that the present design has a more gradual breakdown of head with N_{ss} and that ultimately higher N_{ss} values have presently been achieved. However, curve D, indicates the previously noted result for the two bladed inducer of Reference (13) which achieved $\psi = .0375$, $N_{ss} = 30,000$ at $\phi = 0.08$ rather than the present $\phi = 0.06$. Degradation of head generation for curve D is, however, much more abrupt than the present case indicating a less desirable characteristic.

Figure 26 shows the cavity length to chord ratio (l/c) for the first stage over the range of operating conditions. Typical cavitation patterns started with partial cavitation on

the outer 20 to 50 percent of the back of the blades in combination with tip and gap cavitation. Later the base cavitation developed from the tip toward the base ($l/c > 1.0$). A region of unequal base cavity lengths later developed, typically with $l/c = 1.8$ on one blade and 1.2 on the other. At this point the blades are not yet fully supercavitating but rather are operating supercavitating over the outer 50 to 75 percent of the blade span and base cavitating to the hub. As indicated on Figure 26 fully supercavitating operation is not achieved until $\phi = 0.6$ to 0.7 and $N_{ss} > 22,000$. As suction specific speed is continually increased, cavity lengths grow and reach values of $l/c \approx 3.0$ at around $N_{ss} = 32,500$. In addition a slight amount of face cavitation was observed for some tests. This is indicated on Figure 26. However, it is believed that most of the observed face cavitation resulted from local damage to the blade leading edge which was observed at the conclusion of the test program and is discussed later.

Figure 27 indicates the observed cavitation patterns on the second stage impeller blades. The operating range has been divided into 3 regions. The first region (region A) at moderate first stage suction specific speeds of up to 10,000 to 12,000 had no observable second stage cavitation. The second region (region B) had identical cavitation patterns observable on all four second stage blades. The third region (region C), which made up the majority of the performance map at $N_{ss} > 12,000$, had alternate blade cavitation on the second stage.

By alternate blade cavitation, it is meant that the cavitation patterns on every other of the four blades was identical. The first and second stage impellers were oriented such that the trailing edge of each first stage blade was followed by the leading edge of a second stage blade with a 50° lag. The next second stage blade lagged by 140° and the pattern repeated for the other impeller blades. The largest cavitation regions always appeared on the second stage blades trailing at 50° and in many cases no cavitation at all was observed on the 140° blade even when severe cavitation occurred on the other.

Figures 28 through 32 illustrate some of the numerous cavitation patterns which have been discussed. The cavities which can be seen in the photographs are predominantly the gap and tip cavities which are confined to the region near the test section wall and are much larger than the cavities at smaller spanwise locations on the impeller blades.

Figure 28 illustrates the growth of suction surface tip, gap, and back cavitation at low suction specific speed (~ 5000) for two flow coefficients. The lower flow coefficient results in higher blade angle of attack and therefore higher head and larger cavity size.

Figure 29 shows the more extensive cavitation at N_{ss} in the 12,000 to 16,000 range for two flow coefficients. In the upper photograph of Figure 29, the head generation ($\psi \approx .09$)

by stage 1 is sufficient to suppress stage 2 cavitation. In the lower photograph at higher ϕ and higher N_{ss} , the stage 1 head generation is lower ($\psi \approx .06$) and the second stage is cavitating. This is an interesting comparison in that the second stage head coefficient is about the same ($\psi \approx .095$) for both of these operating conditions.

Figure 30 shows cavitation patterns at high suction specific speeds (20,000-22,000) for two flow coefficients. Again more extensive second stage cavitation occurs at the higher flow coefficient.

Figure 31 shows two views of the first stage cavitation patterns at $\phi = .089$, $N_{ss} = 13,430$. The upper photo shows the full side view of the first stage impeller blade while the lower photograph shows the trailing edge of the same blade as it passes away from the viewer rotating into the plane of the picture at the bottom. In this view one can discern the difference between the larger tip cavity near the test section wall and the smaller (although approximately the same length) base cavity collapsing further in toward the hub.

Figure 32 shows the alternate blade cavitation which occurs on the second stage as previously described. In 32(a) the tandem inducer operating at $\phi = .0745$, $N_{ss} = 20,500$ has a considerable amount of cavitation occurring on the second stage blade following the trailing edge of the first stage blade by 50° . For the same condition, 32(b) shows that the blade following by 140° has virtually no cavitation.

Figure 33 summarizes the effect of suction specific speed on the magnitude of the dominant fluctuating head component divided by first stage head generated. Nearly all the data recorded lie below an envelope which peaks at $\Delta H/H \approx 0.05$ indicating that unsteady head fluctuations were nearly always far less than 5% of the first stage head and would be even smaller if divided by total head generated by both stages. All but one tandem test for which unsteady measurements were made lie below the above mentioned envelope. Some additional runs were made with the first stage alone to measure only unsteady head fluctuation (no inlet and outlet surveys). These tests are indicated by a flag on the data point in Figure 33, and for cases where both isolated and tandem tests are available for the same operating point indicate some tendency toward higher fluctuations in the isolated case.

Figure 34 relates unsteady head fluctuation at the dominant frequency to cavity length to chord ratio on the first stage. It can be seen from this figure that the peak in unsteady fluctuations occurs at cavity length to chord ratio's of just beyond the so-called "range of cavity interference". This is the range of cavity lengths at which the trailing cavity from one blade just reaches the leading edge of the following blade. In Reference (13) it was observed that severe self-induced oscillations occurred in the region just described for both two and three bladed supercavitating inducer stages tested in isolation. Such severe oscillations were never observed in the present test program, however it is interesting

to note that at least the maximum value of the mild fluctuations which were observed occurred at the same cavity interference condition. In addition, the region of maximum fluctuations correlates roughly with that region in which unequal first stage cavity lengths were observed.

Figure 35 indicates the low frequency fluctuating head spectrum non-dimensionalized by shaft rotative frequency since tests were conducted at three different rpm values (2500, 3000 and 3500 rpm). It should be noted that the shaft rotative frequency was always the dominant frequency followed by roughly $1/3$ and twice the shaft frequency. Thus the fluctuations observed appear to be purely related to blade passage frequency rather than any indication of self-induced oscillations due to unsteady cavity length-head relations or rotating stall.

Figures 36 through 39 illustrate the uniformity of axial velocity and head generation with radius for stage 1. Figure 36 shows the non-dimensional axial velocity for three different flow coefficient values at high suction specific speed. Note that the profiles are relatively similar with axial velocity higher at the hub than at the tip for all operating ϕ values. In Reference (13) the axial velocity profiles were non-uniform with considerably higher axial flow at the tip than at the hub. The present empirical reduction of head generation at the tip and increase at the hub (see Table 3) appears to have largely corrected, in fact over corrected the flow uniformity condition.

Figure 37 which shows non-dimensional head generation with radius indicates that a reasonably uniform head generation has been achieved, although slightly more head is still generated at the tip than at the hub. The head generation is most uniform at $N_{ss} = 22,000$ and becomes progressively less uniform at $N_{ss} = 26,000$ and $31,000$. Figure 38 shows the effect of suction specific speed variation on uniformity of axial velocity at nearly constant ϕ . It is apparent that N_{ss} has little influence on this uniformity. The identical observation was made in Reference (13) even though the basic profile was much more non-uniform in (13). Figure 39 shows a similar lack of sensitivity for radial head generation at various suction specific speeds.

Early in the test program, one blade of the first stage impeller suffered a crack near the cantilevered portion of the trailing edge. Figure 40 illustrates the nature of the structural damage. The crack was believed to have started from a small notch near this region, and was purely a result of model construction geometry. A prototype would, of course, have an integral hub and blade arrangement. To guard against further blade damage, two spare blades, which had been previously machined on the multiple head tracing mill, were hand finished and used in place of the original blades. The trailing edges of these blades were also pinned to avoid possible fatigue due to the cantilevered construction. In addition, the test program was conducted at reduced rpm compared to the originally planned 4000 rpm.

At the conclusion of the test program, it was noted that the leading edge of the first stage impeller blades had suffered slight erosion damage and bending. This damage was believed to be the major source of the face cavitation noted previously. Figure 41 indicates the nature of the damage viewed from the back and face of the impeller blade. The white area on the face is due to cavitation erosion of the anodized surface.

7.0 CONCLUSIONS

Based on the experimental and design work reported herein, the following conclusions may be drawn:

1. The first (supercavitating) stage of the tandem inducer configuration tested could operate as high as $N_{ss} = 32,800$ at $\phi = .070$, but the design head coefficient (.0375) and N_{ss} (30,000) could be achieved at only $\phi = .060$.
2. The typical supercavitating inducer $\psi-N_{ss}$ relationship is a gradual reduction of ψ as N_{ss} increases for each ϕ , rather than the precipitous drop-off of more conventional impellers.
3. The fully wetted second stage of a tandem configuration compliments the first stage and results in a reasonably flat $\psi-N_{ss}$ relationship over a broad range of N_{ss} .

4. The present first stage had a much less precipitous head fall-off with N_{ss} than the previous supercavitating models of (12) and (13).
5. The empirical modification reducing tip head and increasing hub head in the design process did significantly improve both axial velocity distribution and head distribution with radius.
6. The empirical design to lower than required local blade cavitation numbers did result in an increase in achievable N_{ss} .
7. The empirical modification to blade pitch to favor higher ϕ operation did not result in achieving design ϕ .
8. It is still not possible to adequately analytically design tandem inducers having supercavitating first stages at least for the very high stagger angles and high suction specific speeds of the present design goals. An empirical approach must be relied upon. The present design techniques invariably result in inducers which operate at lower than design ϕ .
9. The second stage of the present tandem configuration almost always operated with alternate blade cavitation patterns.

10. The tandem inducer having a supercavitating first stage can operate over a wide range of flow coefficients and suction specific speeds with head fluctuations of less than 5% of the first stage generated head.
11. The region of maximum head fluctuation ($\Delta H/H$) for the present tandem inducer configuration occurred at a frequency equal to the shaft rotational frequency and corresponded to regions of unequal cavity length to chord ratio on the first stage and to cavity lengths near the "interference" length extending just beyond the leading edge of the following blade. Pressure fluctuations appeared somewhat lower for the tandem configuration than for an isolated first stage.
12. A model trailing-edge crack was due to model construction technique and does not apply to the prototype, however, model leading edge damage could be significant to the prototype. In any case, the structural problems of thin supercavitating sections should not be underestimated.

REFERENCES

1. Daily, J. W., "Theory of Turbomachinery," Chapter 8 in Engineering Hydraulics, H. Rouse, Ed., Wiley, 1961.
2. Ross, C. C. and Banerian, G., "Some Aspects of High Suction Specific Speed Pump Inducers," Transactions ASME, Vol. 78, Number 8, 1956.
3. Pinkel, I. I., et al., "Conference on Selected Technology for the Petroleum Industry," NASA SP-5053, Chapter 6, Pump Technology, December 1965.
4. Acosta, A. J., "An Experimental Study of Cavitating Inducers," Trans. 2nd Symp. on Naval Hydrodynamics, ONR Publication ACR-38, 1958.
5. Hartmann, M. J., and Soltis, R. F., "Observations of Cavitation in a Low Hub-Tip Ratio Axial Flow Pump," ASME Paper No. 60-Hyd-14, March 1960.
6. Tura, T., Discussion of Ref. 4 by Acosta, Trans. 2nd Symp. on Naval Hydrodynamics, ONR Pub. ACR-38, 1958.
7. Soltis, R. F., "Some Visual Observations of Cavitation in Rotating Machinery," NASA TN D-2681, July 1965.
8. Crouse, James E. and Sandercock, Donald M., "Blade-Element Performance of Two Stage Axial Flow Pump with Tandem Row Inlet Stage," NASA TN D-3962, May 1967.
9. Sandercock, D. M., and Crouse, J. E., "Design and Overall Performance of a Two-Stage Axial-Flow Pump with a Tandem-Row Inlet Stage," NASA TN D-2879, March 1965.
10. Soltis, R. F., Urasek, D. C., and Miller, M. J., "Blade-Element Performance of a Tandem-Bladed Inducer Tested in Water," NASA TN D-5562, November 1969.

11. Soltis, R. F., Urasek, D. C., and Miller, M. J., "Overall Performance of a Tandem-Bladed Inducer Tested in Water," NASA TN D-5134, May 1969.
12. Contractor, D. N., and Etter, R. J., "An Investigation of Tandem Row High Head Pump Inducers, Interim Report - Phase I," HYDRONAUTICS, Incorporated Technical Report 703-4, May 1969.
13. Etter, R. J., "An Investigation of Tandem Row High Head Pump Inducers - Final Report," HYDRONAUTICS, Incorporated Technical Report 703-9, May 1970.
14. Eisenberg, P. and Tulin, M. P., "Cavitation," Chapter 12 in Handbook of Fluid Dynamics, V. L. Streeter, Ed. McGraw-Hill, 1961.
15. Yeh, H., "An Actuator Disc Analysis of Inlet Distortion and Rotating Stall in Axial-Flow Turbomachines," Journal of the Aeronautical Sciences, Vol. 26, No. 11, 1959.
16. Stripling, L. B., and Acosta, A. J., "Cavitation in Turbo-Pumps, Part I," ASME Hydraulics Division Paper No. 61-WA-11, November 1961.
17. Acosta, A. J., and Hollander, A., "Remarks on Cavitation in Turbomachines," CIT Report 79.3, October 1959.
18. Wade, R. B., and Acosta, A. J., "Investigation of Super-cavitating Cascades," ASME Journal Basic Engr. Paper 66-WA/FE-25, December 1967.
19. Etter, R. J. and F. J. Turpin, "Cavitating Pump Instabilities in the J-2 LOX System," HYDRONAUTICS, Incorporated Technical Report 7021-1, June 1971.
20. Knapp, R. T., "Recent Investigations of the Mechanics of Cavitation and Cavitation Damage," ASME Paper 54-A-106, ASME, Annual Meeting, New York, November 1954.

21. Auslaender, J., "The Linearized Theory for Supercavitating Hydrofoils Operating at High Speeds Near a Free Surface," HYDRONAUTICS, Incorporated Technical Report 001-5, June 1961.
22. Yim, B., "Supercavitating Cascades with Constant Pressure Cambered Blades," HYDRONAUTICS, Incorporated Technical Report 703-2, July 1967 (NASA CR-90426).
23. Yim, B., "The Higher Order Theory of Supercavitating Cascades with Constant Pressure Cambered Blades," HYDRONAUTICS, Incorporated Technical Report 703-3, October 1967. (NASA CR-91444).
24. Wislicenus, F. G., "Fluid Mechanics of Turbomachinery," Volumes I and II, Dover Publications, New York, 1965.
25. Stepanoff, A. J., "Centrifugal and Axial Flow Pumps," 2nd Ed. John Wiley and Sons, New York, 1967.
26. Bowerman, R. D., "The Design of Axial-Flow Pumps," Trans. ASME, Vol. 78, No. 8, 1956.
27. Johnson, V. E., Jr., "Theoretical and Experimental Investigation of Supercavitating Hydrofoils Operating Near the Free Water Surface," N.A.S.A. Technical Report R-93, 1961.
28. Hsu, C. C., "On the Flow Past a Supercavitating Cascade of Cambered Blades," HYDRONAUTICS, Incorporated Technical Report 703-5, February 1969. (NASA CR-100773)
29. Hsu, C. C., "On the Flow Past a Cascade of Partially Cavitating Cambered Blades," HYDRONAUTICS, Incorporated Technical Report 703-6, March 1969.
30. Hsu, C. C., "On Flow Past a Supercavitating Cascade of Cambered Blades," Journal of Basic Engineering, Trans. ASME, Series D, Vol. 94, No. 1, March 1972.

31. Hsu, C. C., "Some Second-Order Results for Flow about Supercavitating Lifting Hydrofoils," *Journal of Basic Engineering*, Trans. ASME, Series D, Vol. 94, No. 1, March 1972.
32. Tyson, H. N., Jr., "Three-Dimensional Interference Effects of a Finite Number of Blades in an Axial Turbomachine," C.I.T. Report E19.1, November 1952.
33. Etter, R. J. and Van Dyke, P., "Three Dimensional Flow Field from a Radial Vortex Filament in a Cylindrical Annulus," HYDRONAUTICS, Incorporated Technical Report 703-7, December 1969.
34. Papir, A. N., Axial Pumps of Water-Jet Propulsion Systems, Sudostroyeniye Publishing House; Leningrad, U.S.S.R., 1965.
35. Etter, R. J., and Hsu, C. C., "An Investigation of Tandem-Row High-Head Pump Inducers - Interim Report Phase II," HYDRONAUTICS, Incorporated Technical Report 703-8, February 1970.
36. Jackson, E. D., "Supercavitating LOX Inducer-Final Report," Rocketdyne Report R-8747, July 1971.
37. Streeter, V. L., "Steady Flow in Pipes and Conduits," Chapter VI in Engineering Hydraulics (H. Rouse, ed.), John Wiley and Sons, New York, 1950.
38. Rouse, H. and Hassan, M. M., "Cavitation-Free Inlets and Contractions," *Mechanical Engineering*, Vol. 71, No. 3, 1949.
39. Jackson, E. D., "A Brief Review of the Supercavitating Inducer and Its Potential Use with a J-2 Oxidizer Pump," Rocketdyne Report TMR 0115-3094, September 1970.

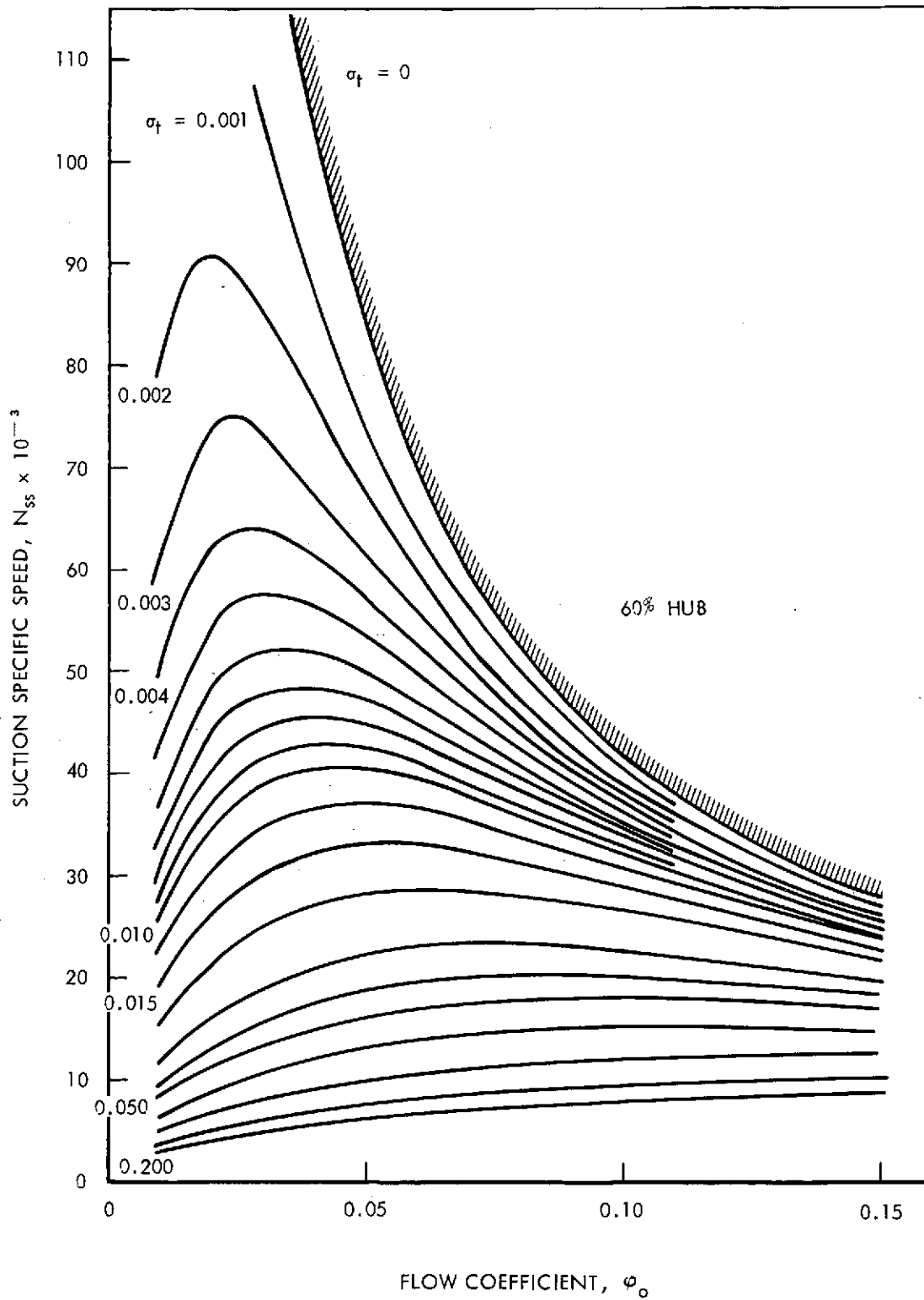


FIGURE 1 - INFLUENCE OF FLOW COEFFICIENT ON RELATIONSHIP BETWEEN SUCTION SPECIFIC SPEED AND TIP CAVITATION NUMBER FOR A 0.60 HUB / DIAMETER RATIO

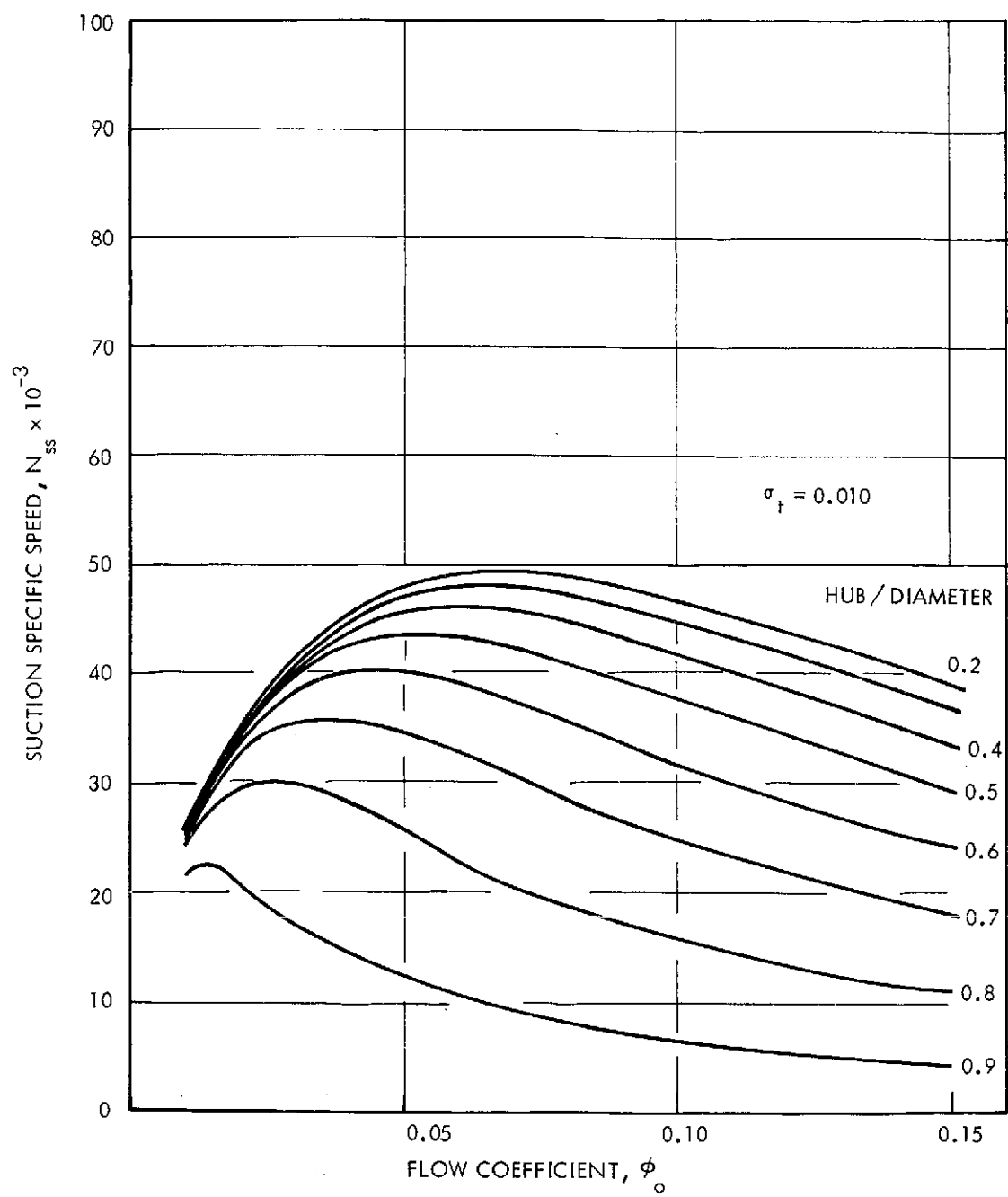


FIGURE 2 - INFLUENCE OF HUB / DIAMETER RATIO AND FLOW COEFFICIENT ON SUCTION SPECIFIC SPEED AT $\sigma_t = 0.010$.

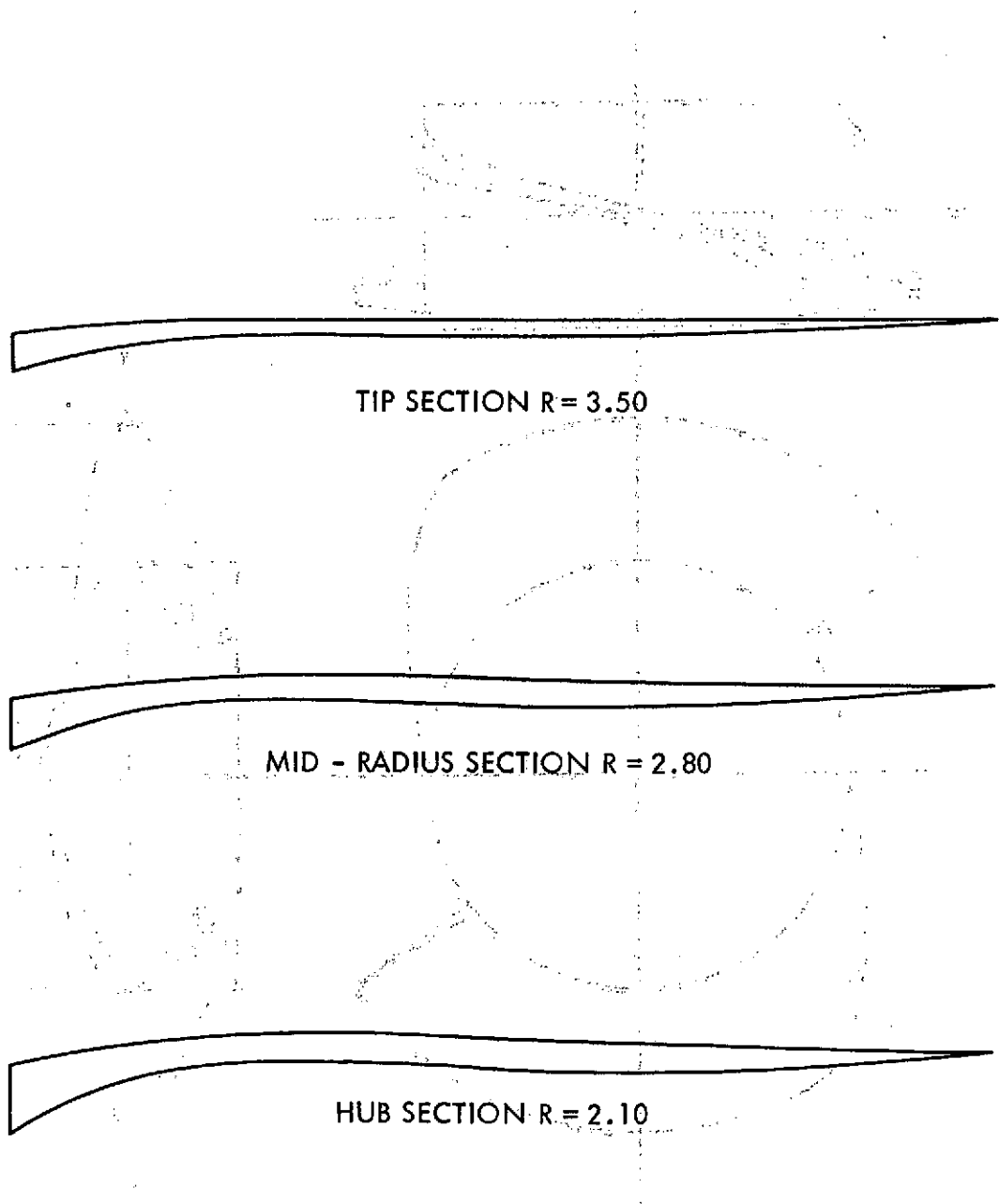


FIGURE 3 - FIRST STAGE IMPELLER SECTIONS - FULL SCALE

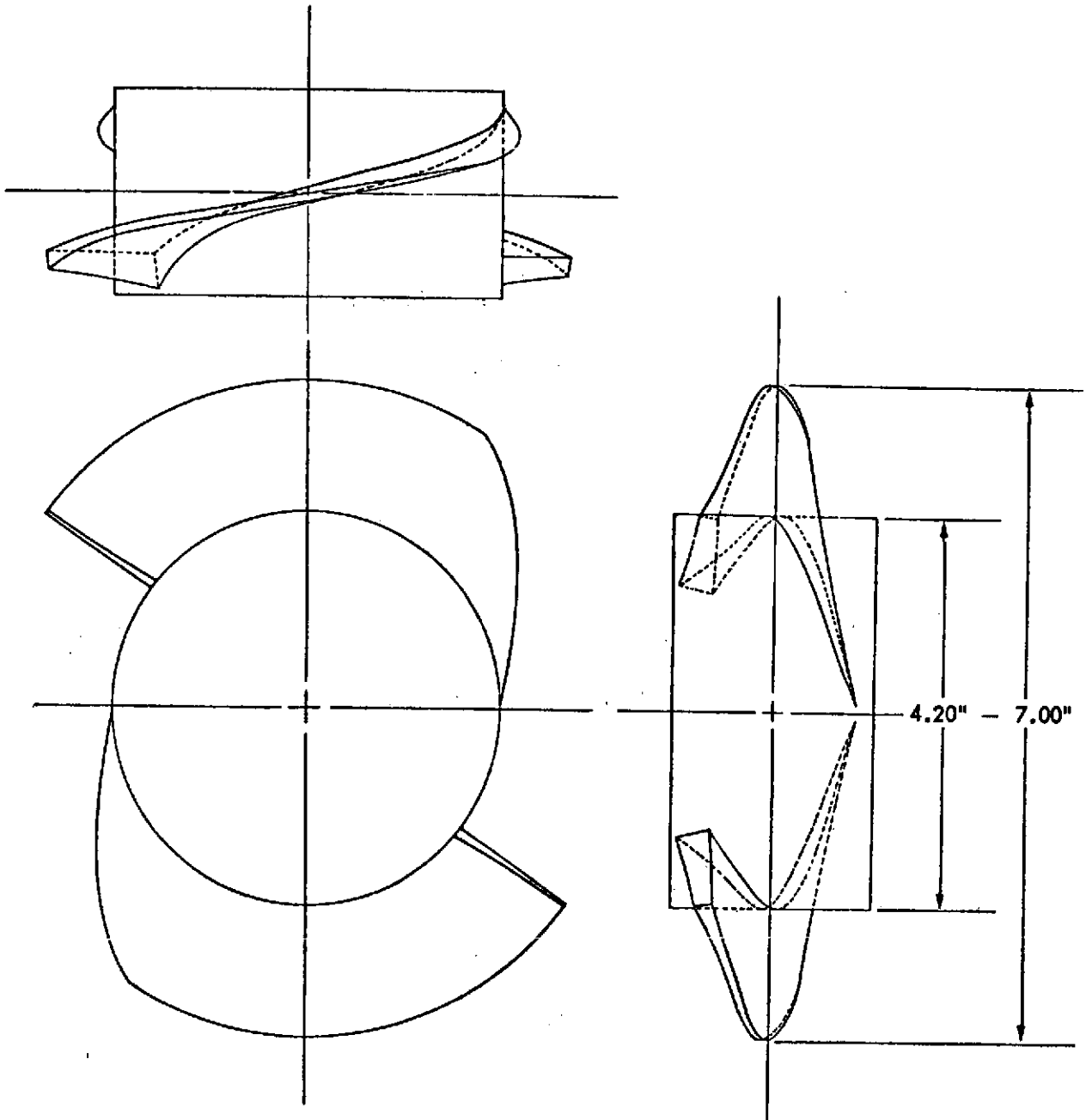


FIGURE 4 - THREE VIEWS OF THE SUPERCAVITATING STAGE HAVING FIVE-TERM CAMBERED BLADE FORMS, CONSTANT CHORD LENGTH AND A $60 \frac{1}{2}$ HUB RATIO

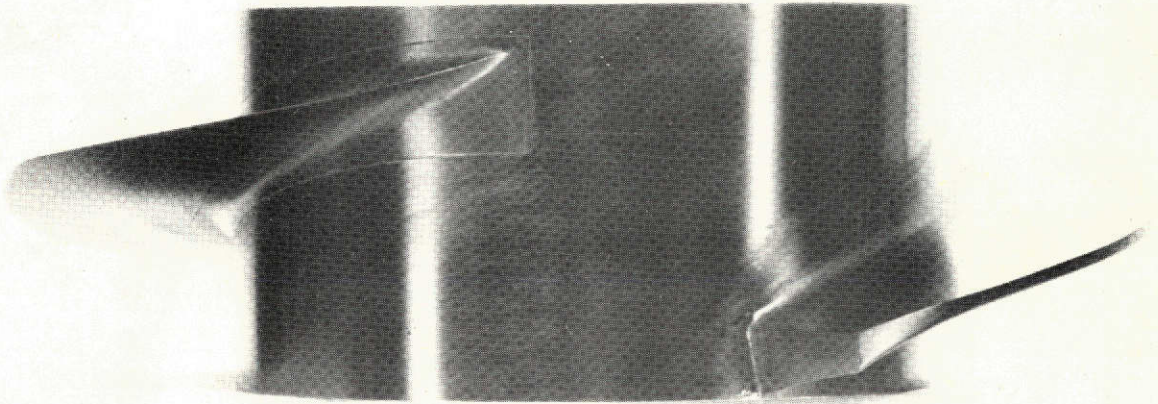


FIGURE 5 - FIRST STAGE (SUPER-CAVITATING) IMPELLER

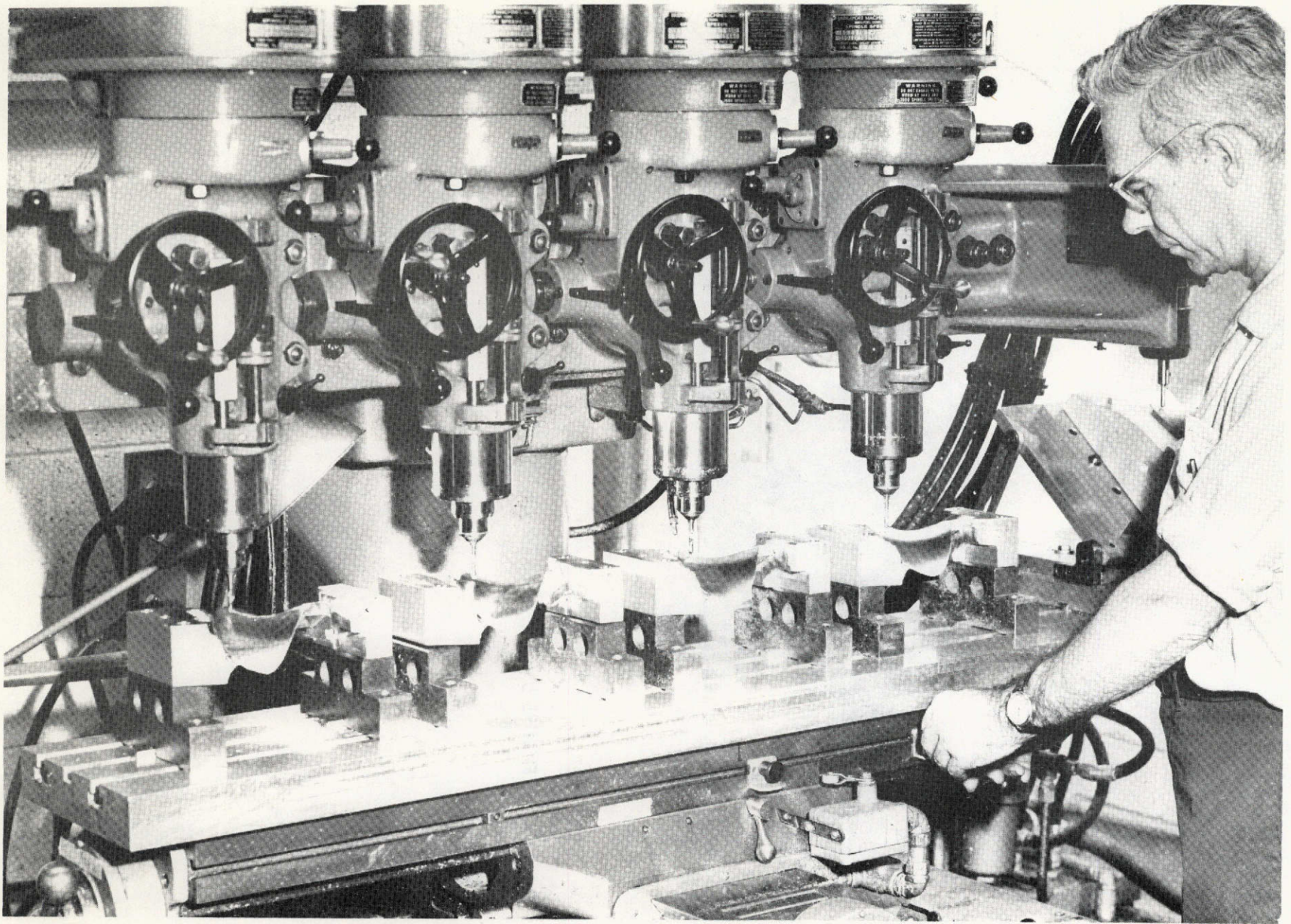


FIGURE 6 - MULTIPLE MILLING OF IMPELLER BLADES FROM PATTERN

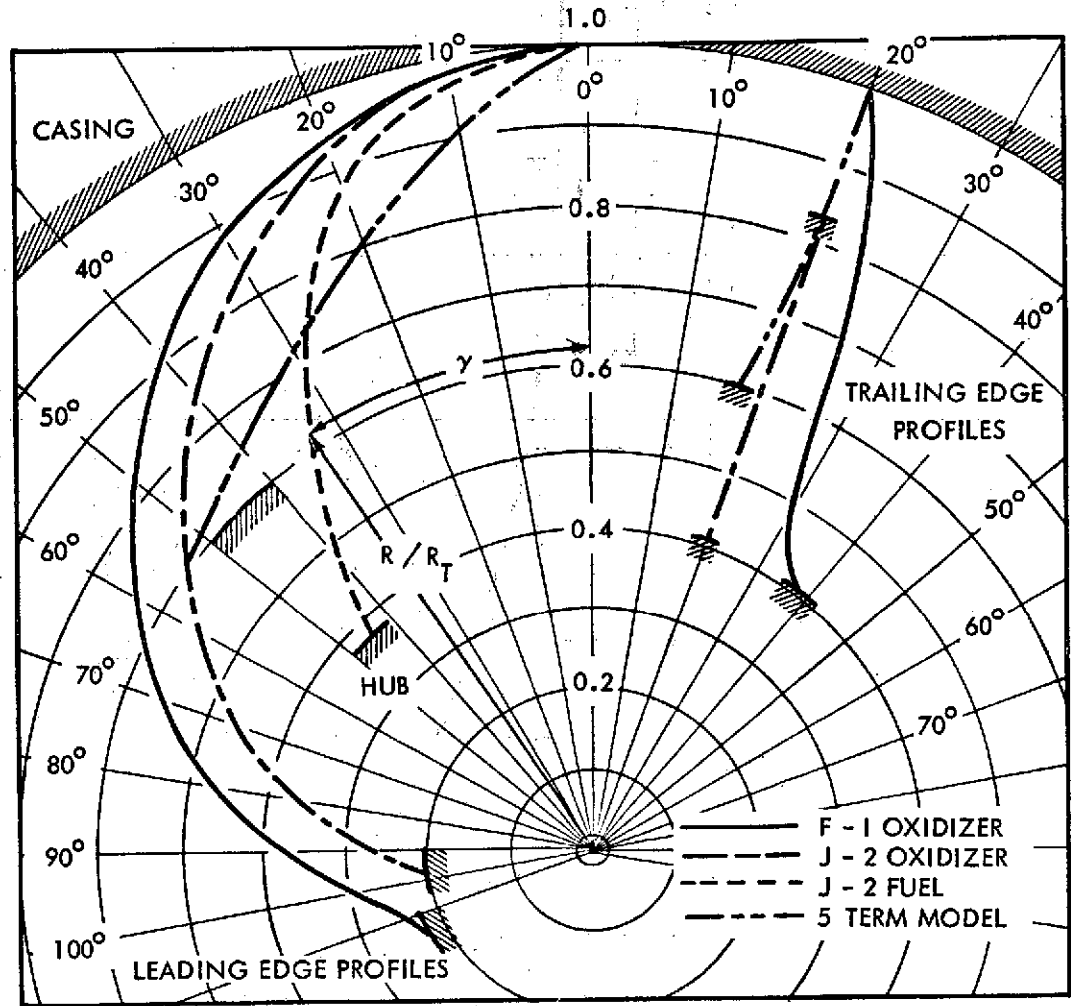


FIGURE 7 - NON-DIMENSIONAL COMPARISON OF LEADING AND TRAILING EDGE PROFILES USED IN SATURN V ENGINE INDUCERS TO 5 - TERM CAMBERED MODEL WITH CONSTANT CHORD LENGTH (WRAP NOT PROPERLY INDICATED)

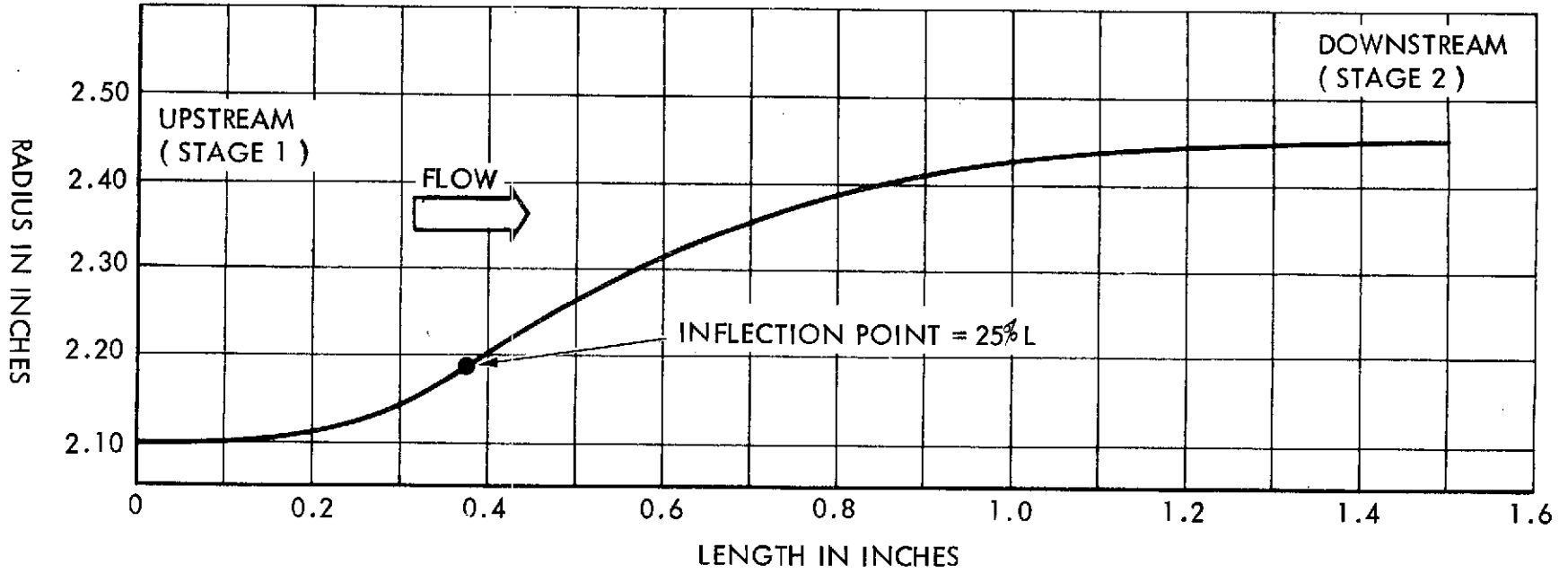


FIGURE 8 - CUBIC ARC TRANSITION SHAPE

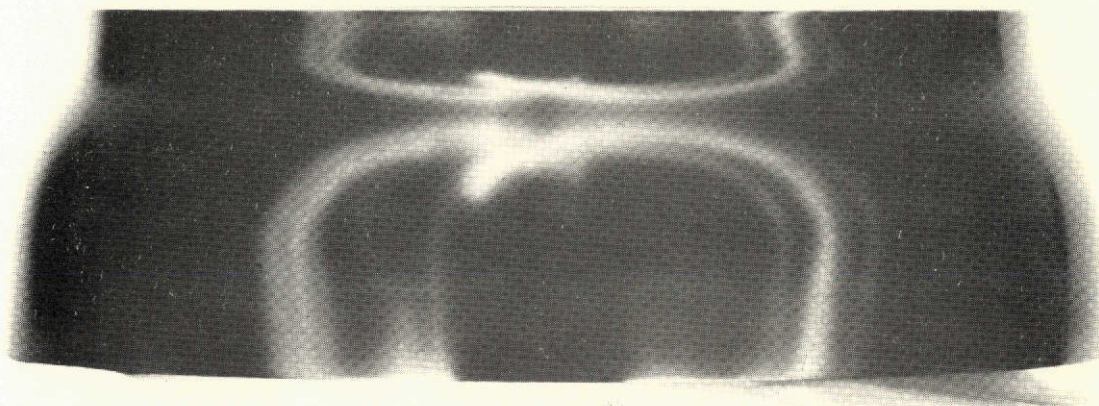


FIGURE 9 - CUBIC ARC TRANSITION SECTION

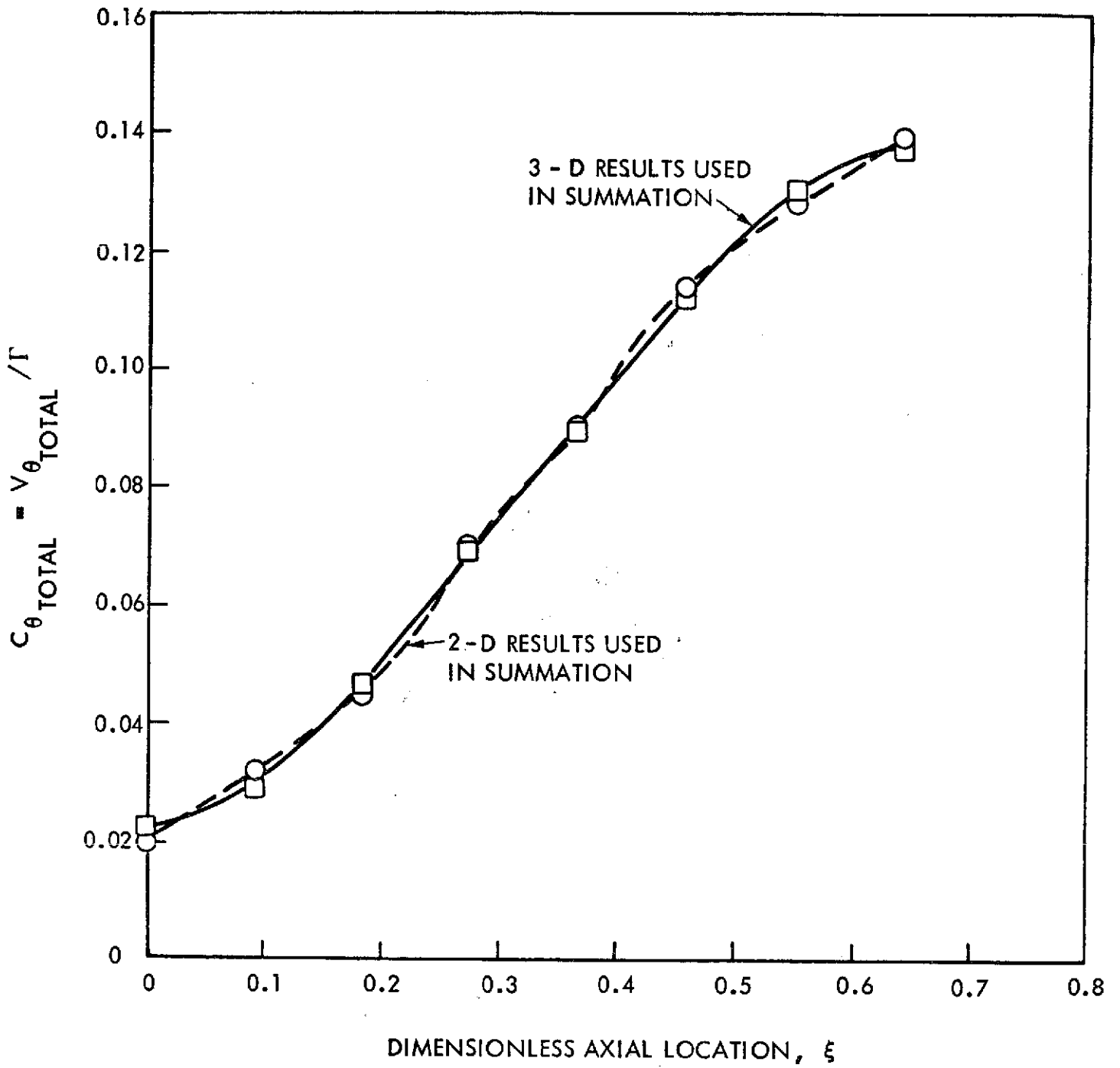


FIGURE 10 - SAMPLE INTERFERENCE STREAMLINE CALCULATION USING BOTH TWO AND THREE DIMENSIONAL RESULTS

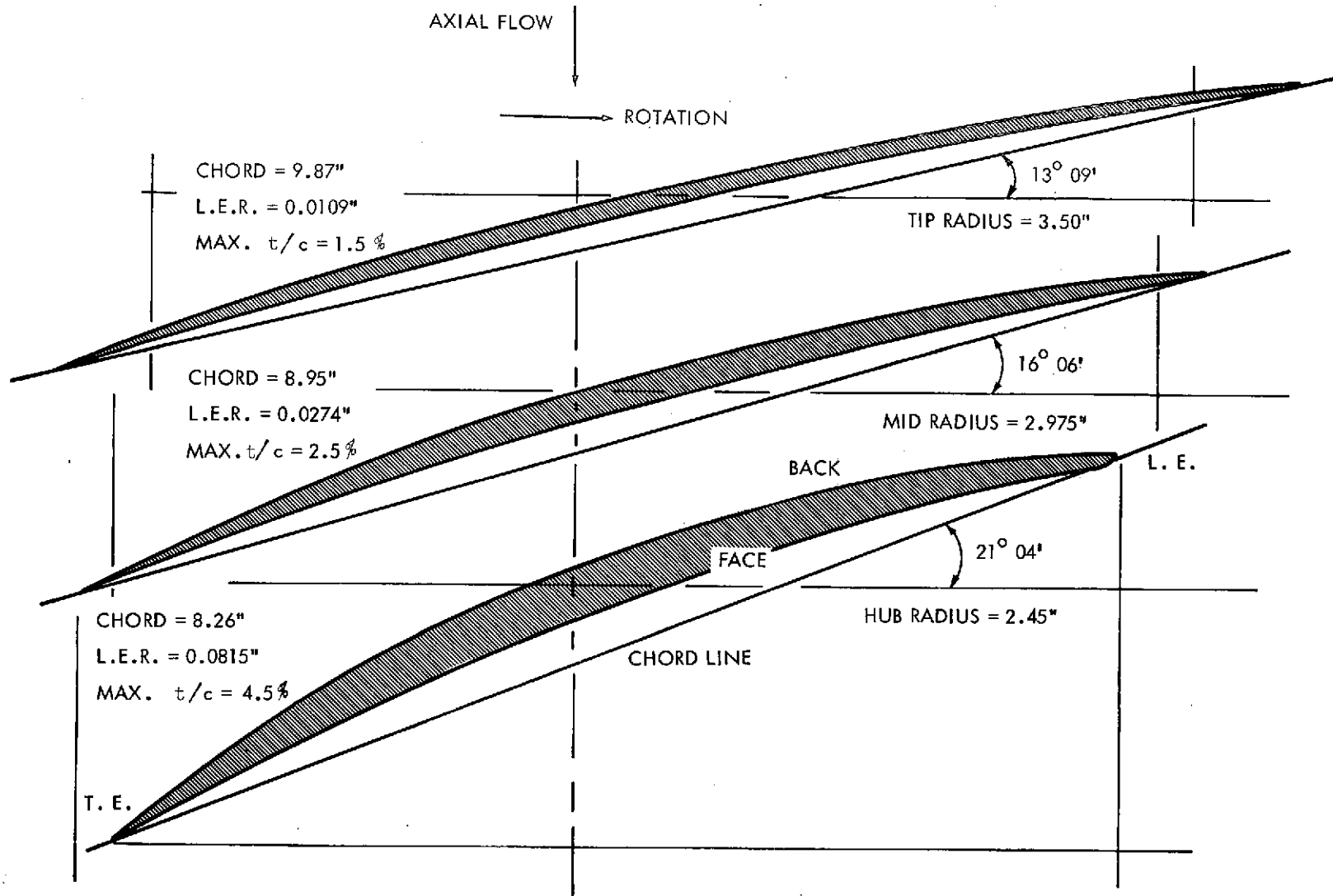


FIGURE 11- SECOND STAGE TWO DIMENSIONAL BLADE PROFILES AT THREE RADII.
(FOUR BLADES, 0.70 HUB)

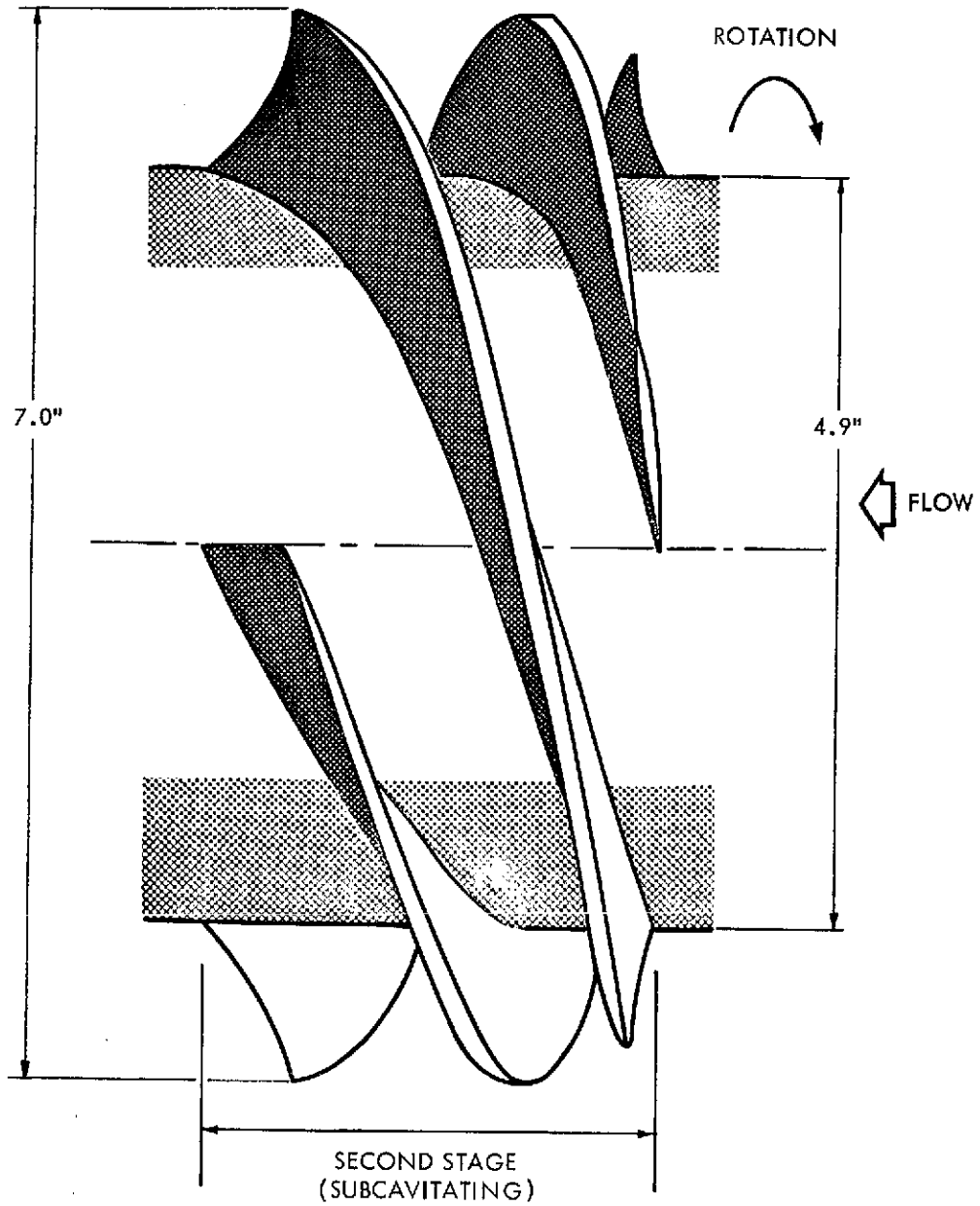
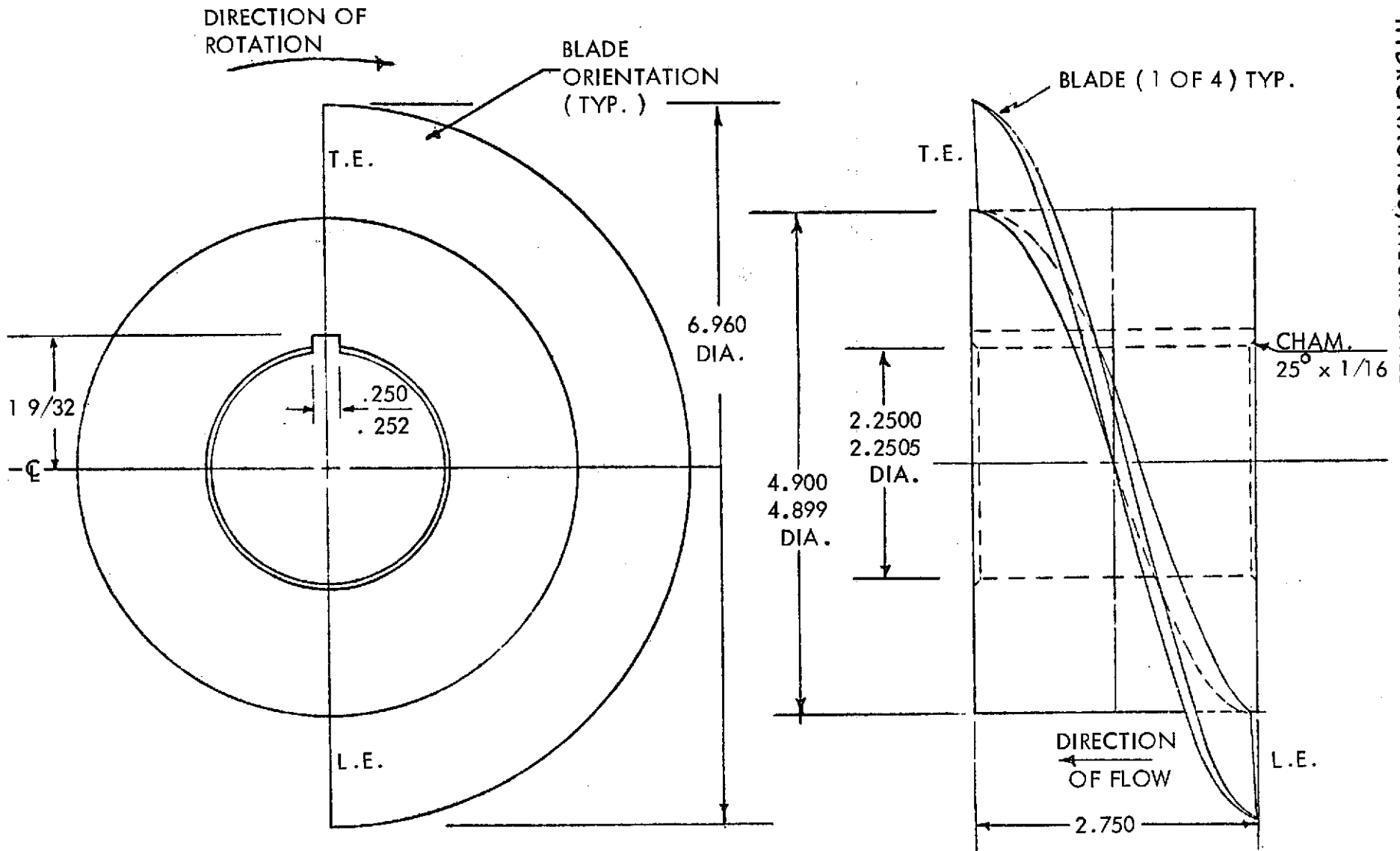


FIGURE 12 - SECOND STAGE IMPELLER USING FOUR BLADES AND 0.70 HUB



HYDRONAUTICS, INCORPORATED

FIGURE 13 - SECOND STAGE DETAIL

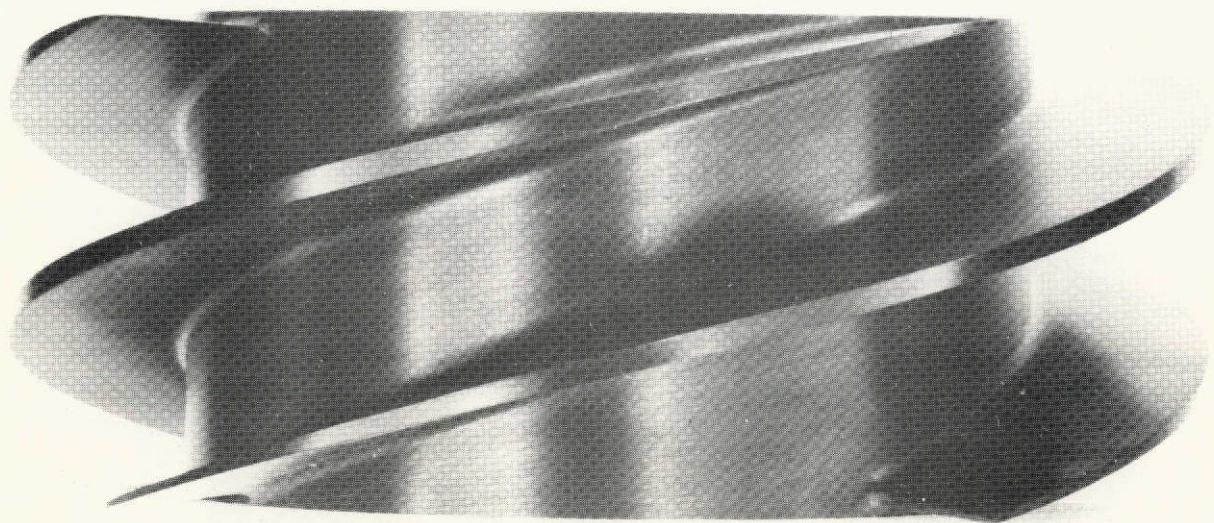


FIGURE 14 - SECOND STAGE (SUB-CAVITATING) IMPELLER



FIGURE 15 - TWO STAGE INDUCER ASSEMBLY

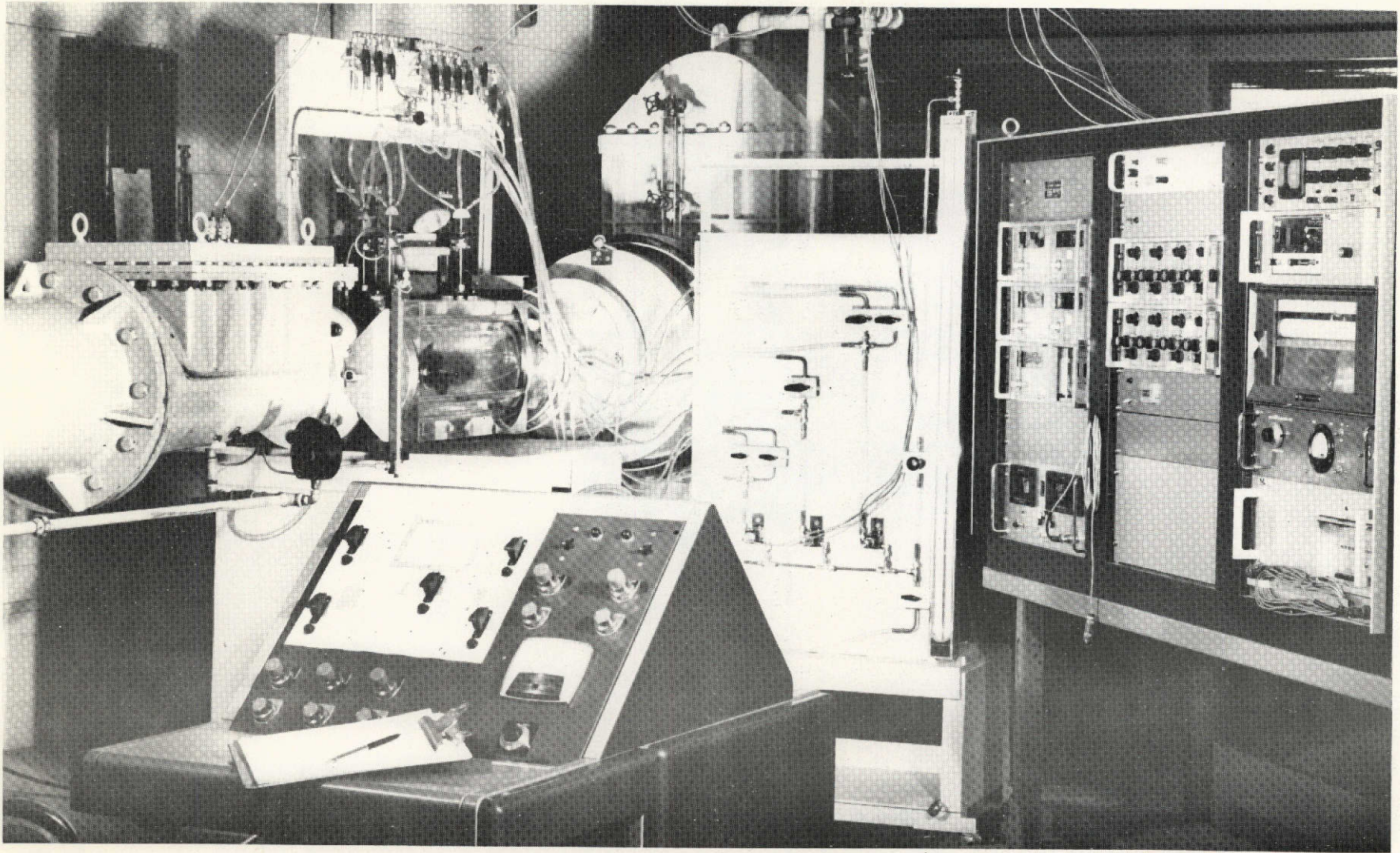


FIGURE 16 - PUMP LOOP INSTRUMENTATION, CONTROL, AND DATA ACQUISITION SYSTEMS.

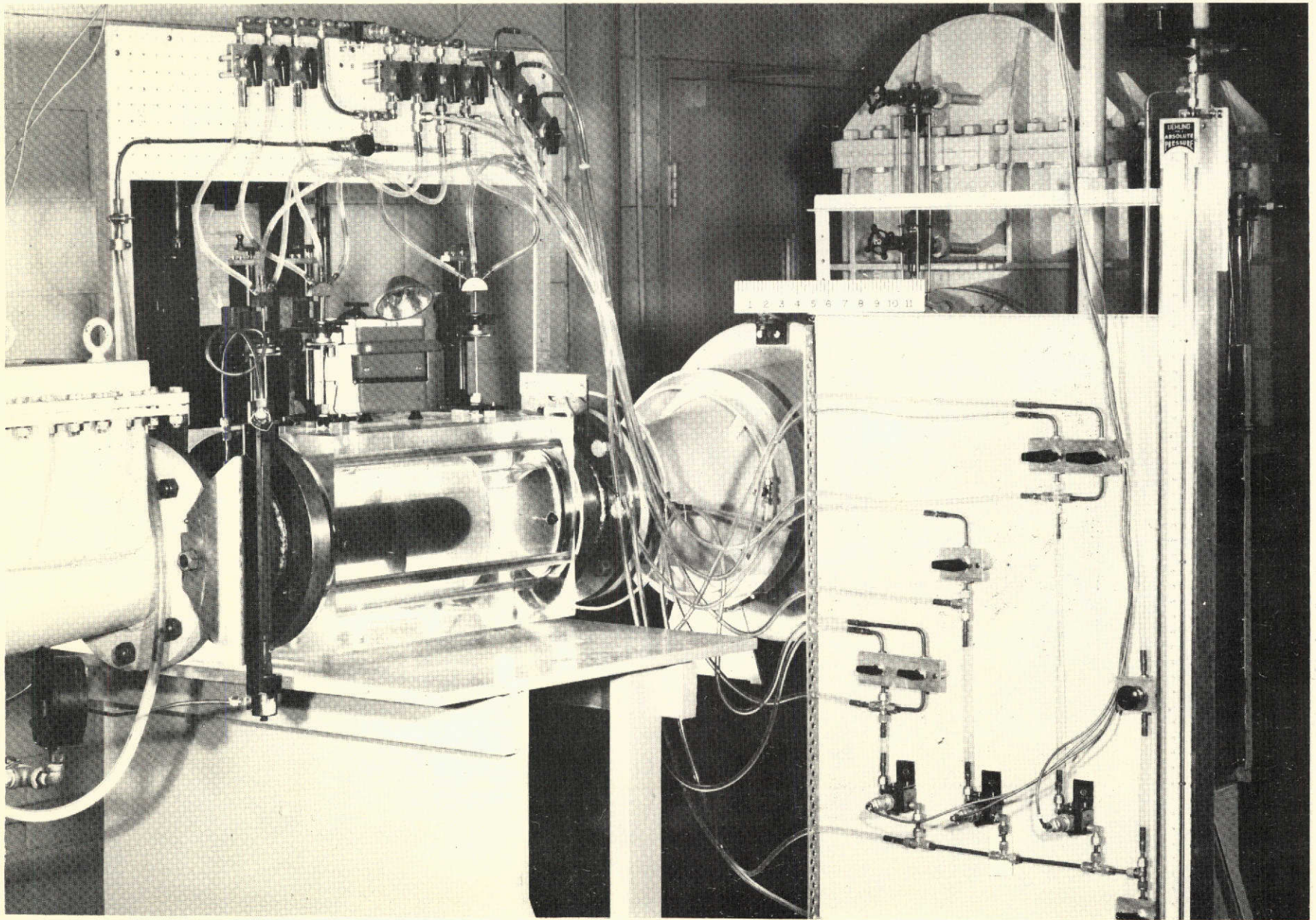


FIGURE 17 - PUMP LOOP TEST SECTION

HYDRONAUTICS, INCORPORATED

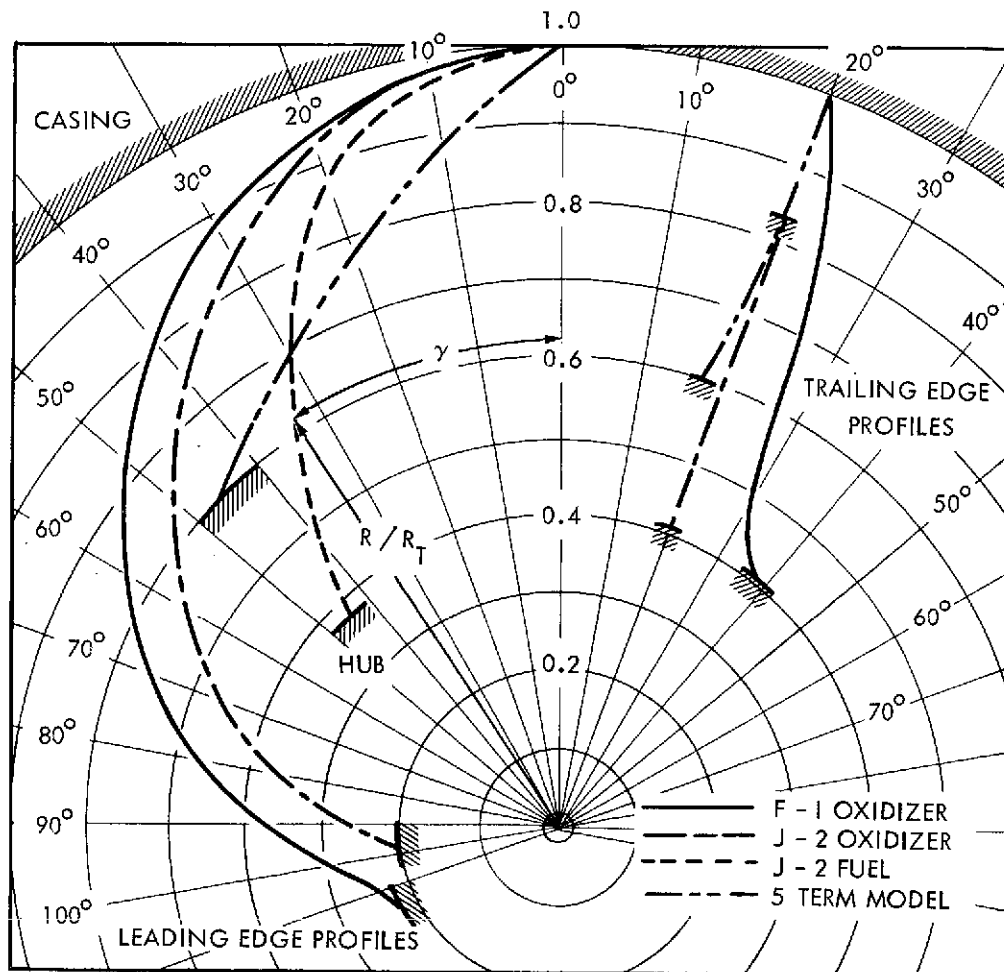


FIGURE 18 - COMPARISON OF LEADING AND TRAILING EDGE PROFILES USED IN SATURN V ENGINE INDUCERS TO 5 - TERM CAMBERED MODEL WITH CONSTANT CHORD LENGTH

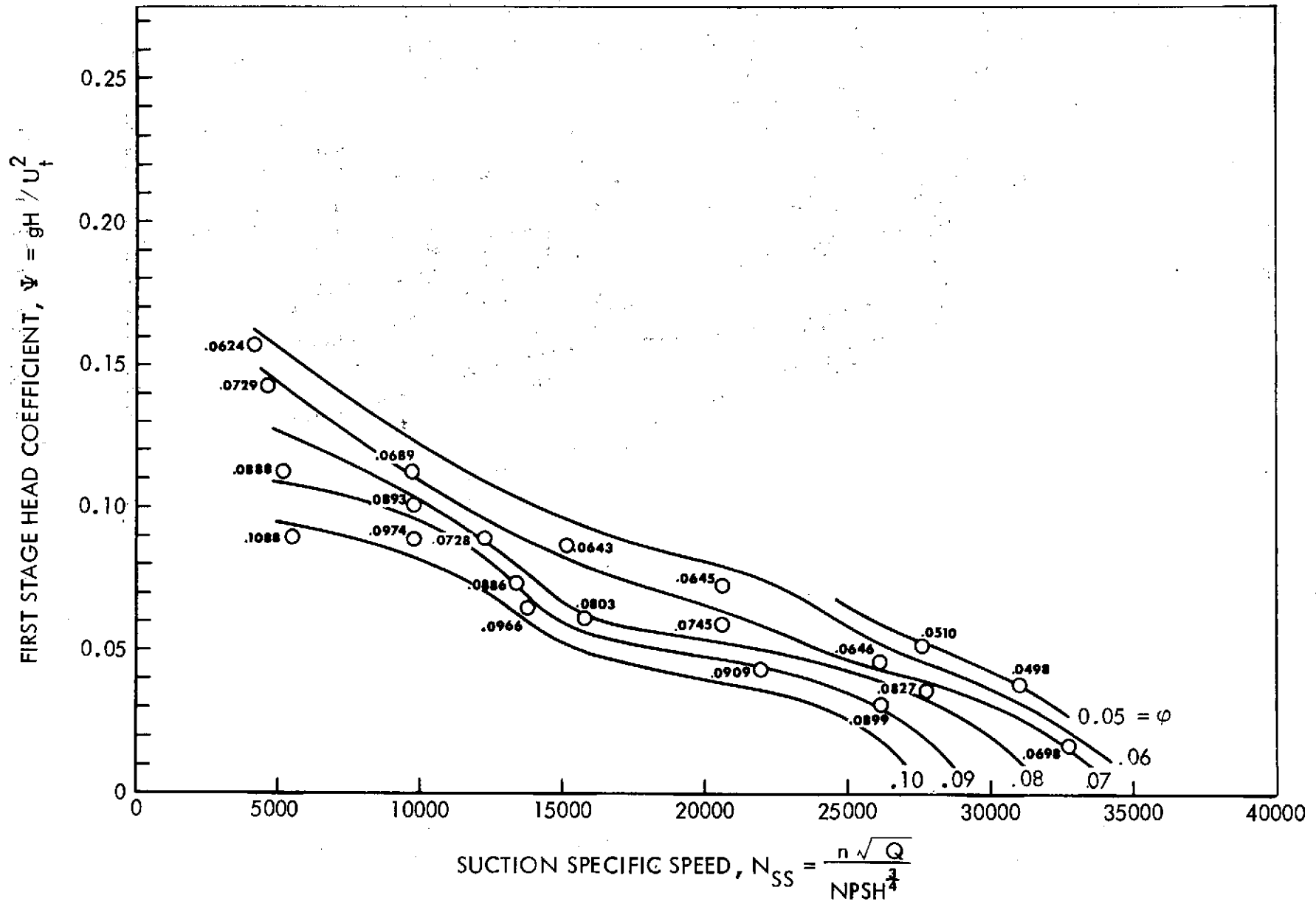


FIGURE 19 - FIRST STAGE HEAD COEFFICIENT AS INFLUENCED BY SUCTION SPECIFIC SPEED AND FLOW COEFFICIENT

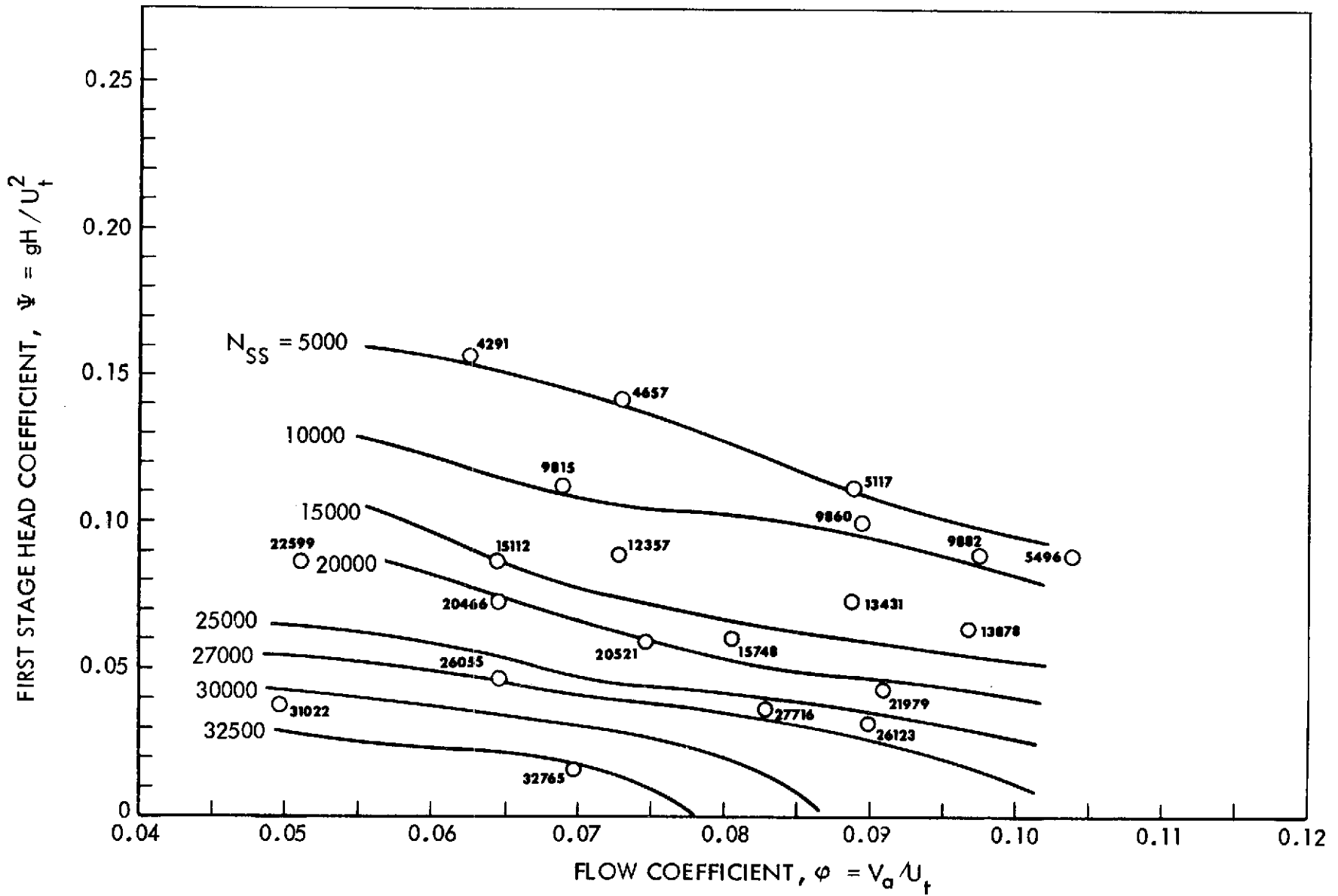


FIGURE 20 - FIRST STAGE HEAD COEFFICIENT - FLOW COEFFICIENT RELATIONSHIP FOR VARIOUS SUCTION SPECIFIC SPEEDS

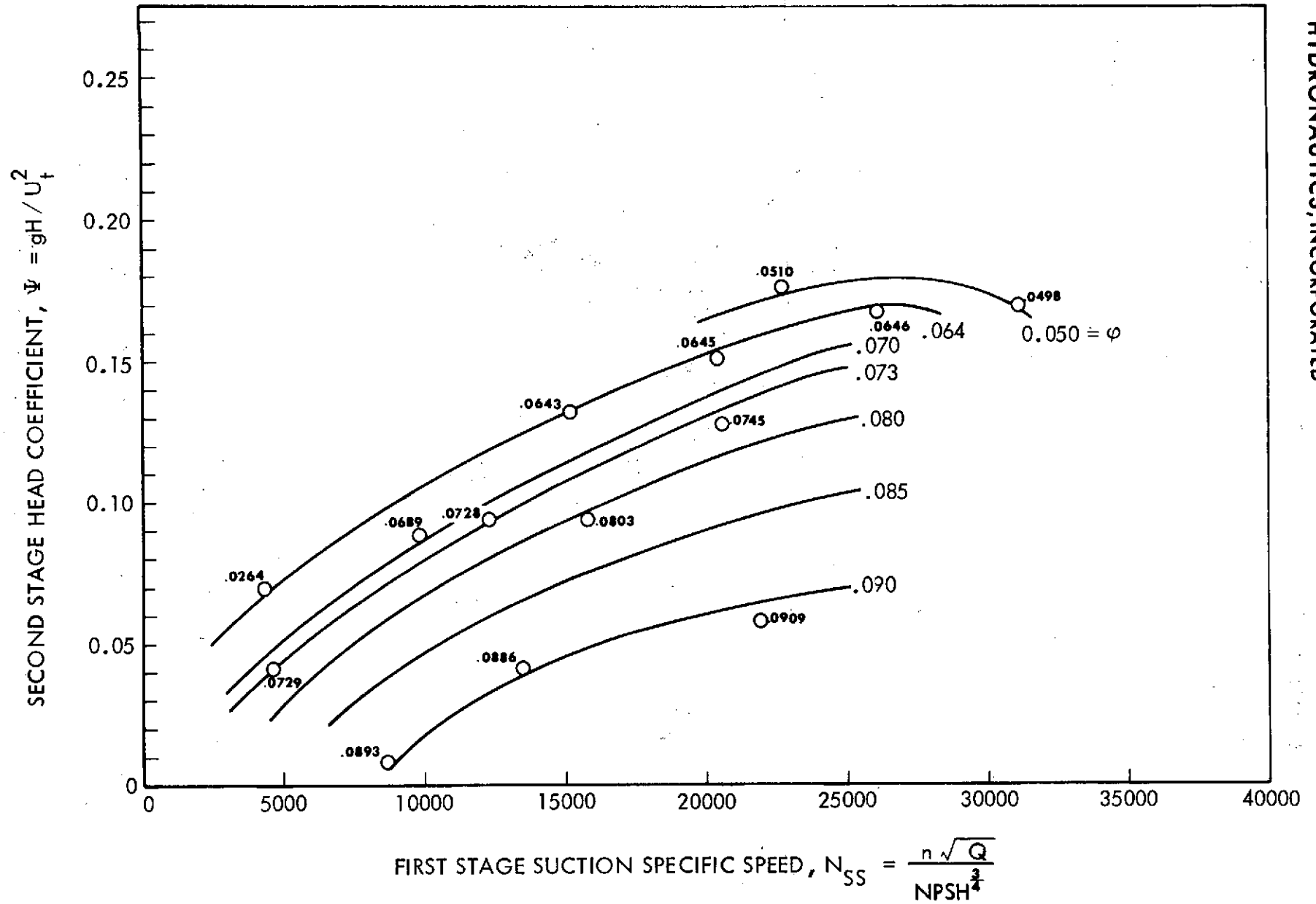


FIGURE 21 - SECOND STAGE HEAD COEFFICIENT AS INFLUENCED BY FIRST STAGE SUCTION SPECIFIC SPEED AND FLOW COEFFICIENT

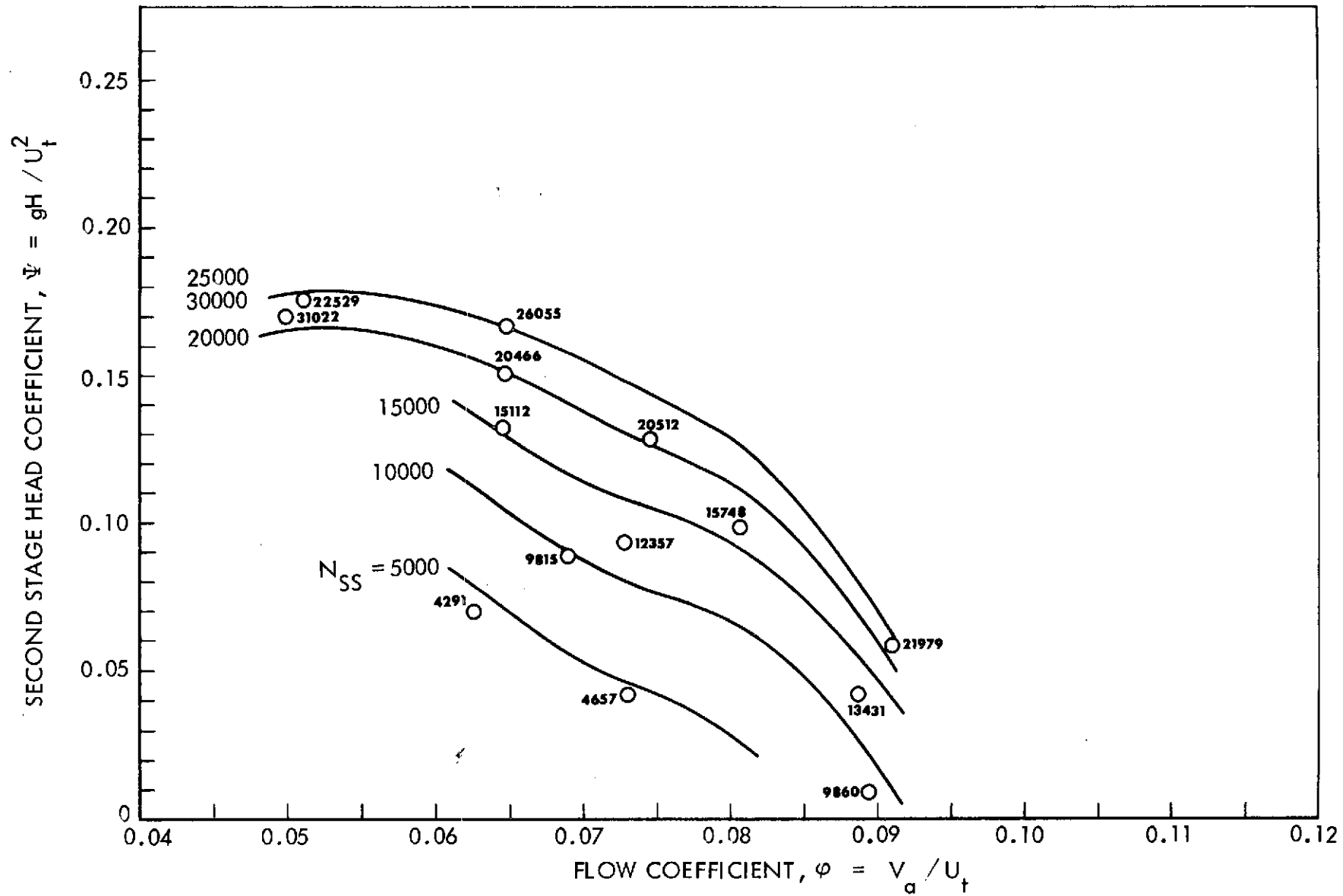


FIGURE 22 - SECOND STAGE HEAD COEFFICIENT - FLOW COEFFICIENT RELATIONSHIP FOR VARIOUS FIRST STAGE SUCTION SPECIFIC SPEEDS

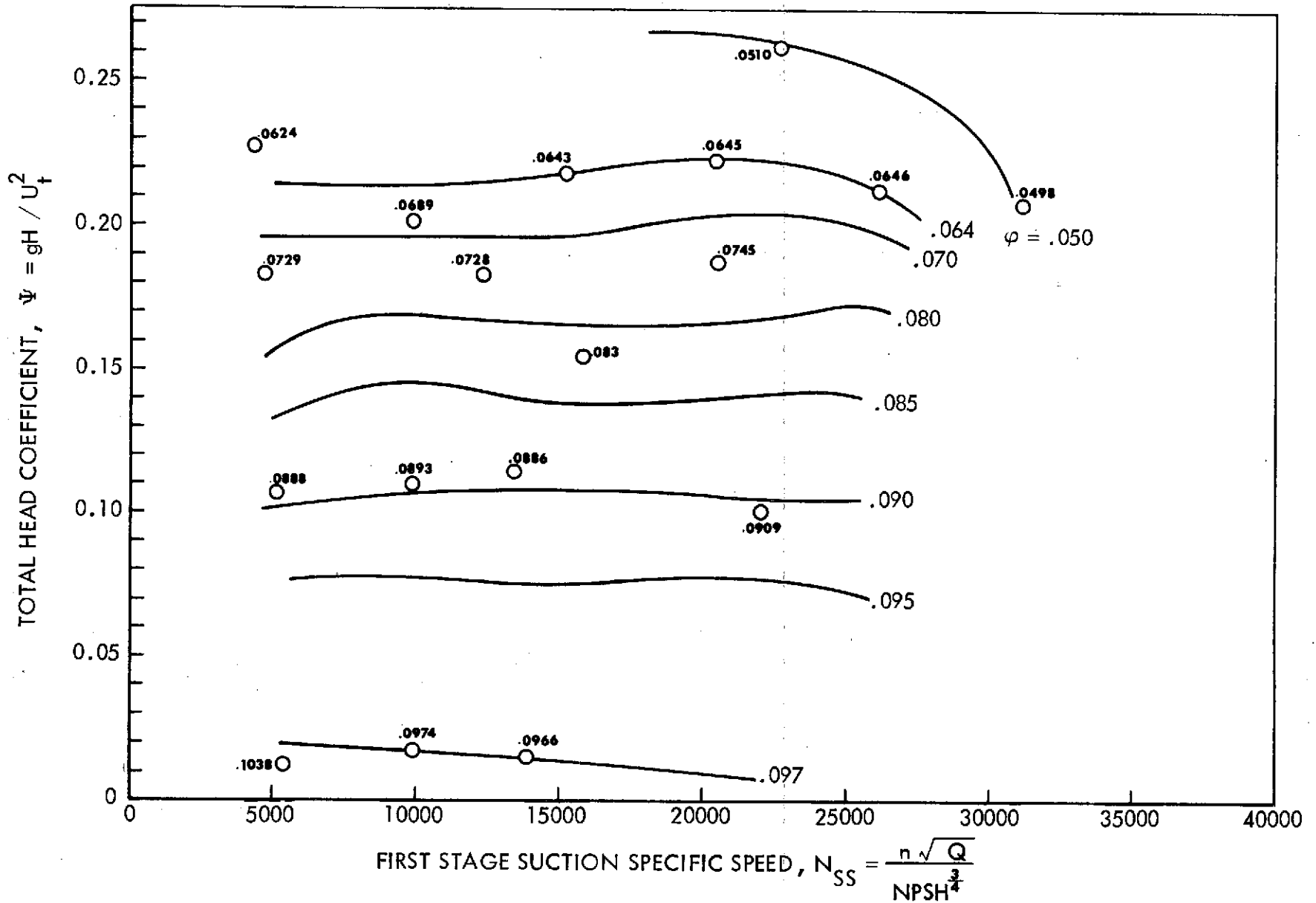


FIGURE 23 - TANDEM HEAD COEFFICIENT AS INFLUENCED BY SUCTION SPECIFIC SPEED AND FLOW COEFFICIENT

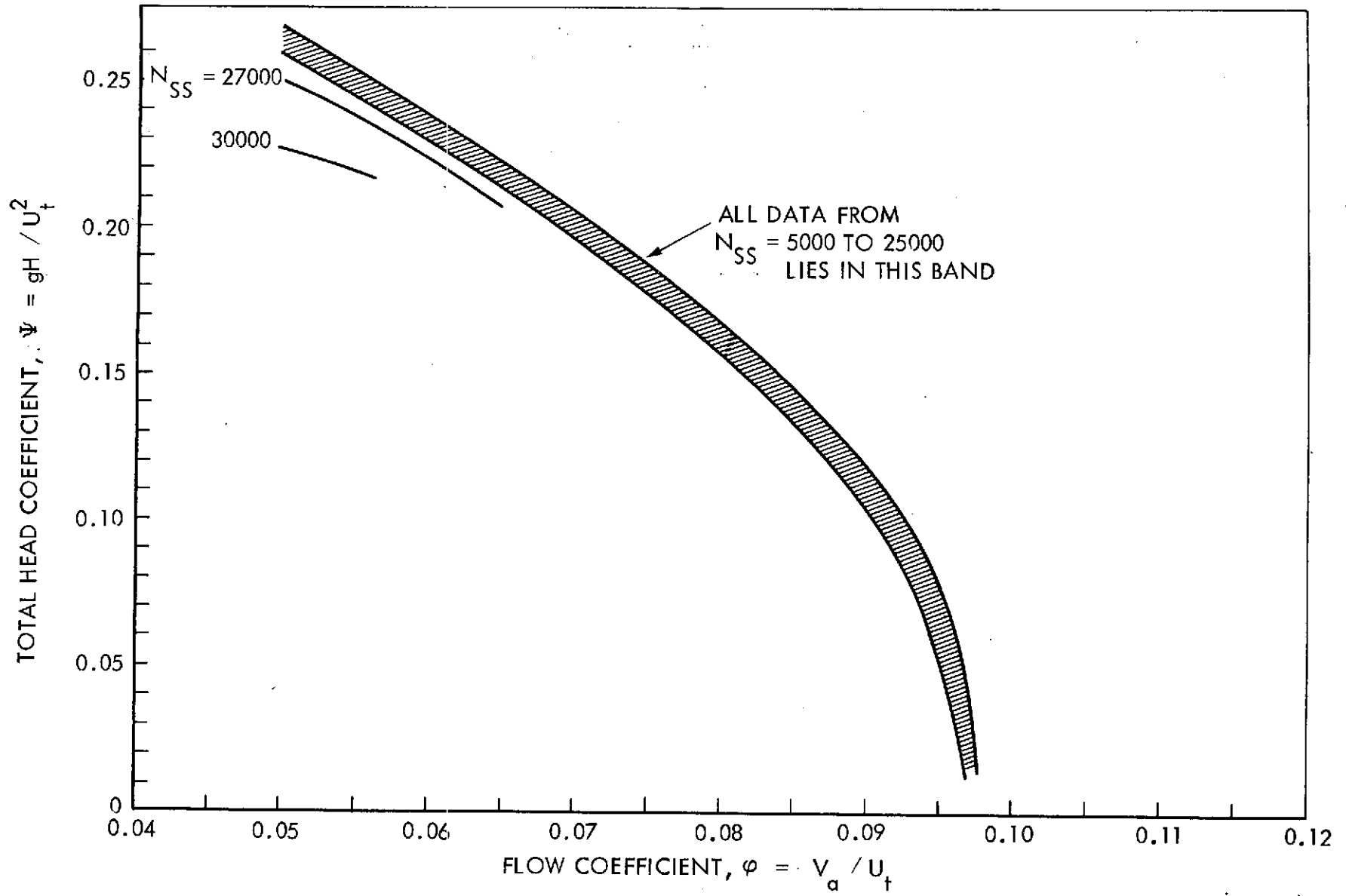


FIGURE 24 - TANDEM HEAD COEFFICIENT - FLOW COEFFICIENT RELATIONSHIP

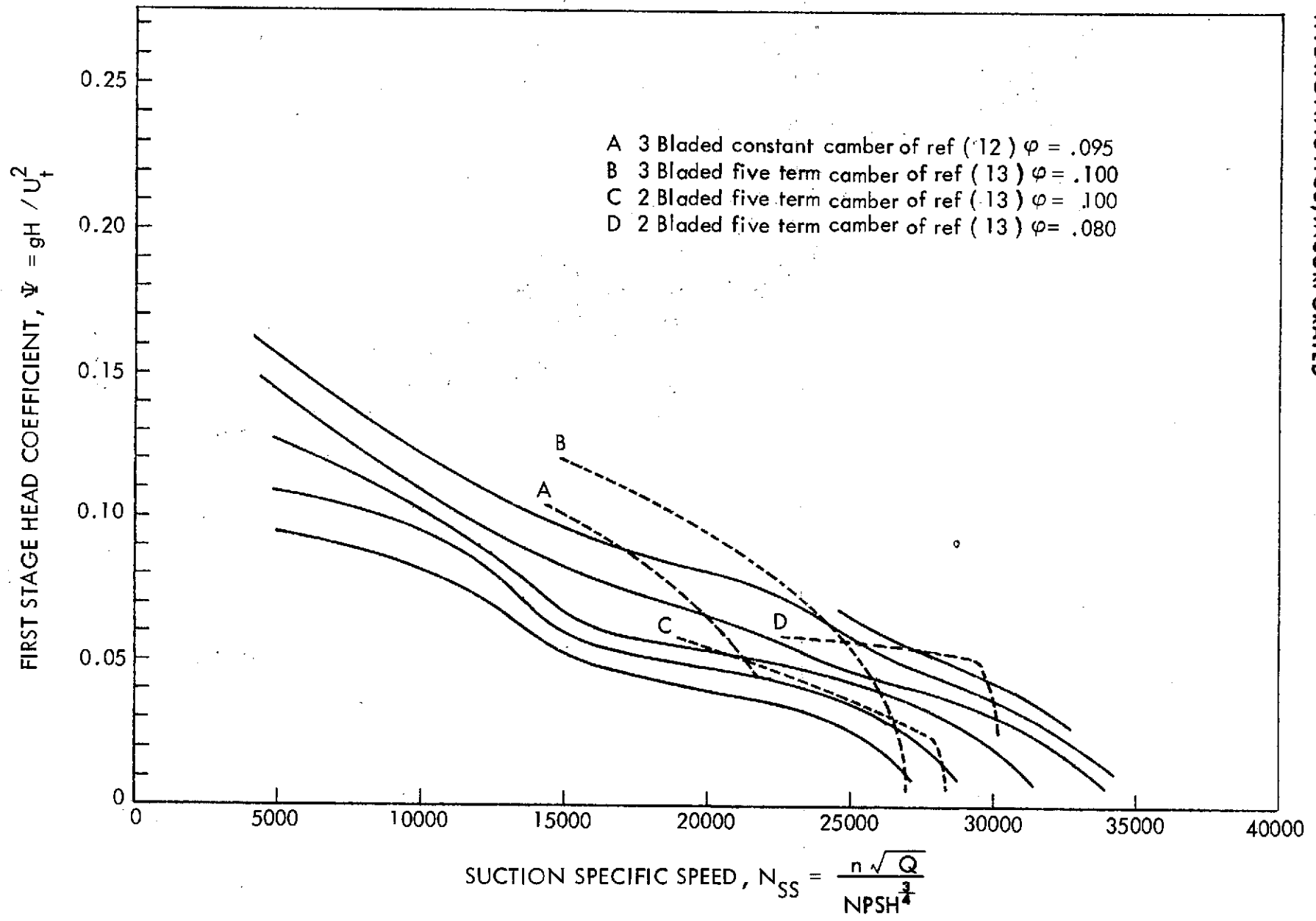


FIGURE 25 - FIRST STAGE SUCTION PERFORMANCE COMPARED TO OTHER SUPERCAVITATING INDUCERS

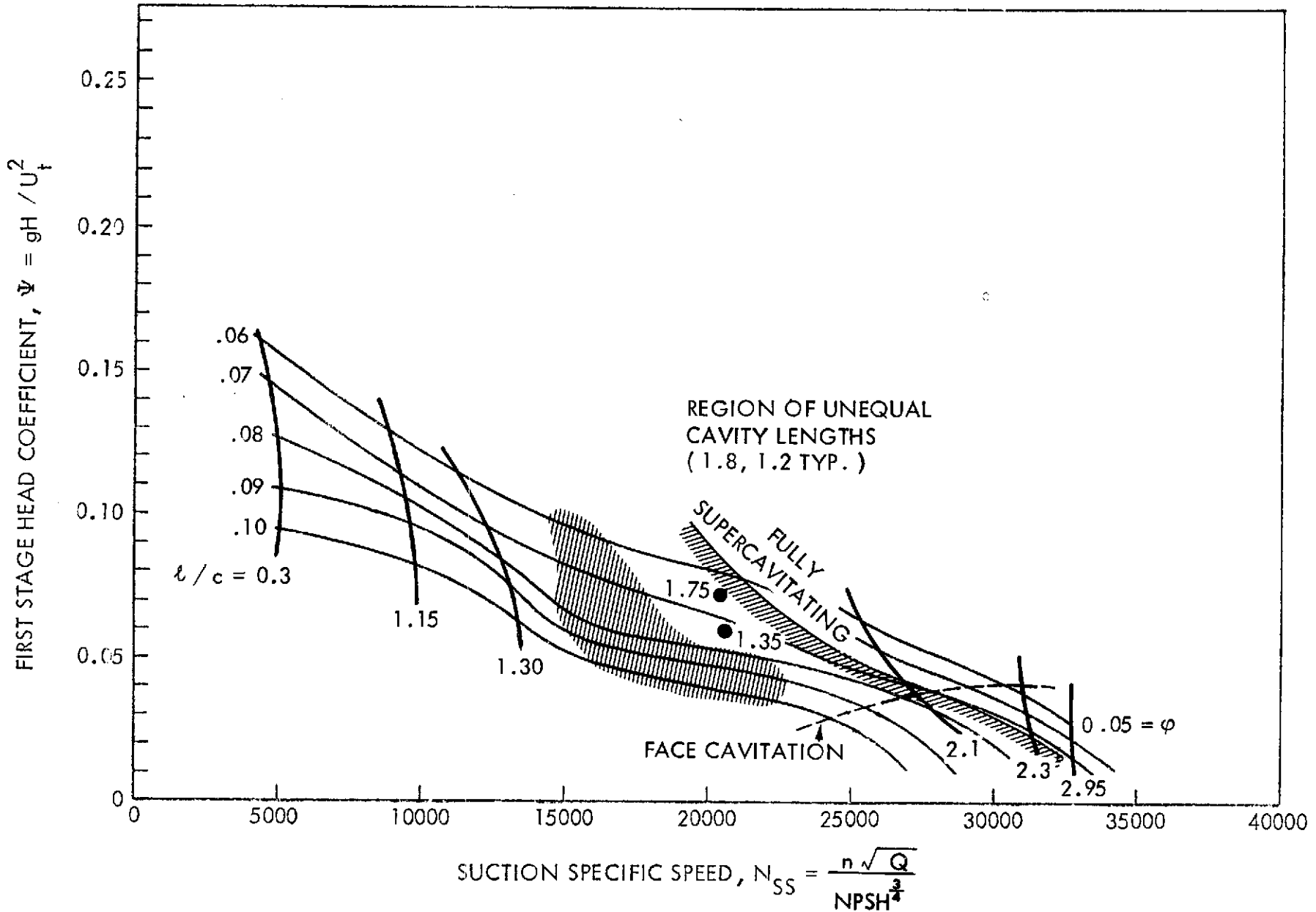


FIGURE 26 - FIRST STAGE CAVITY LENGTHS AND CAVITATION PATTERNS

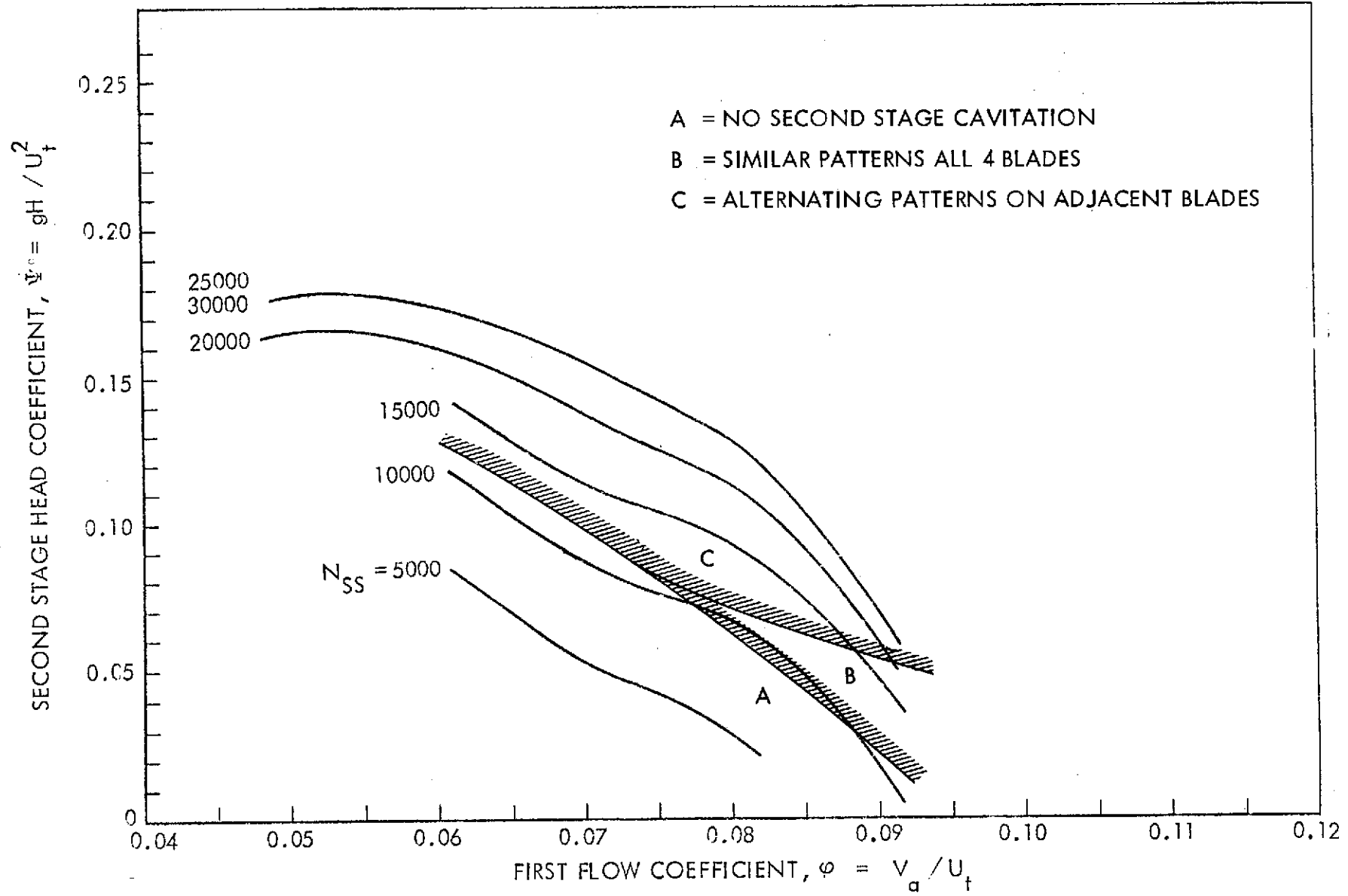
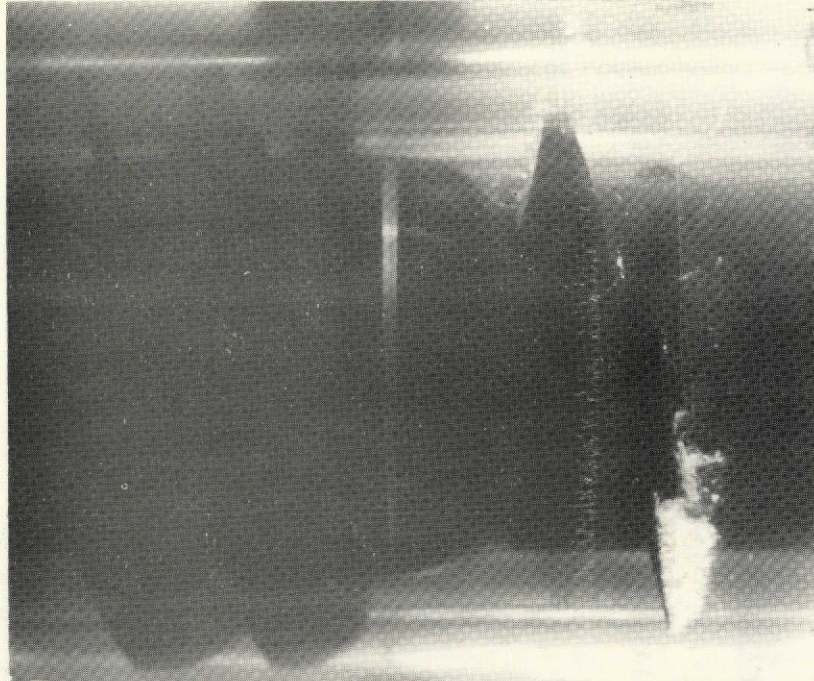
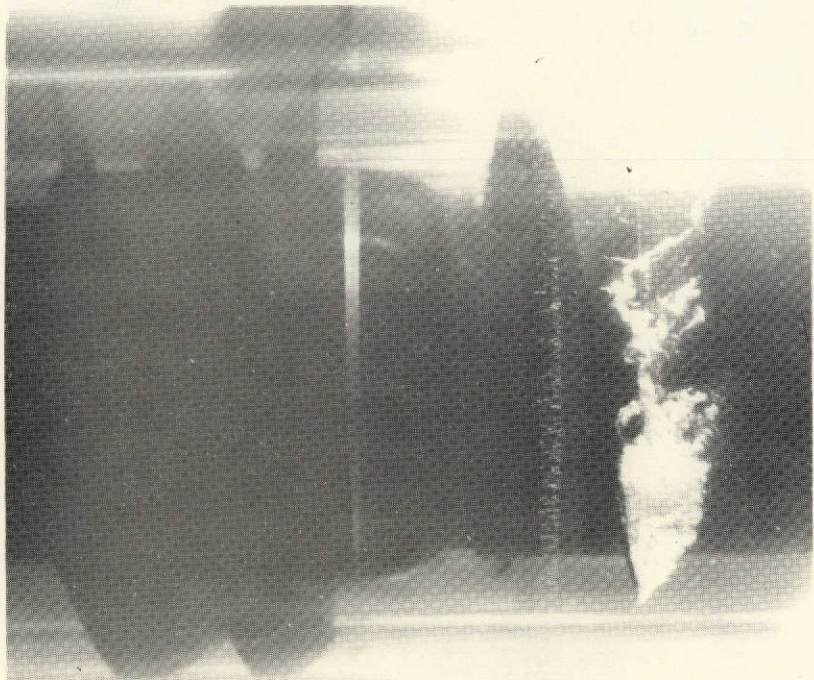


FIGURE 27 - SECOND STAGE CAVITATION PATTERNS



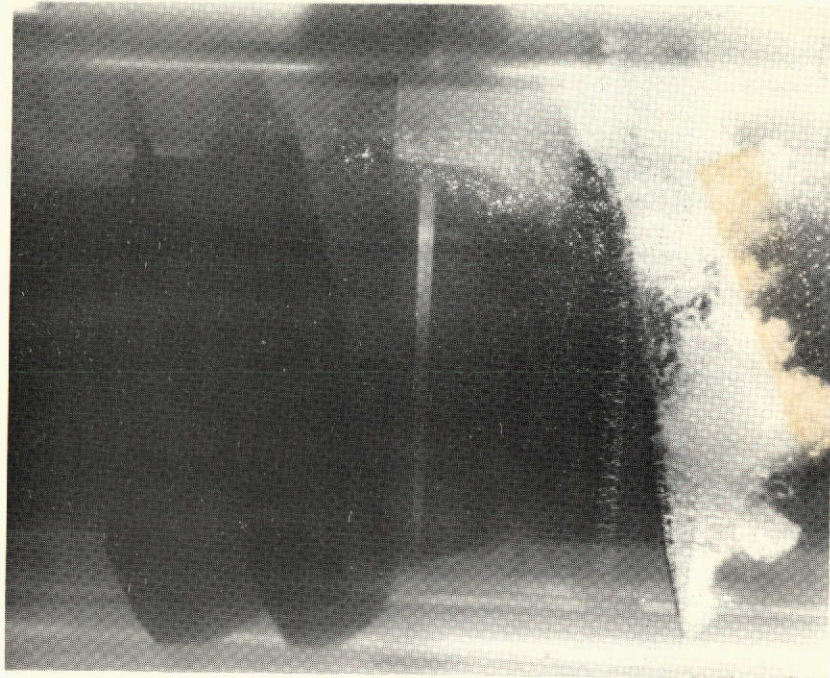
$\phi = .089 \quad N_{SS} = 5120$



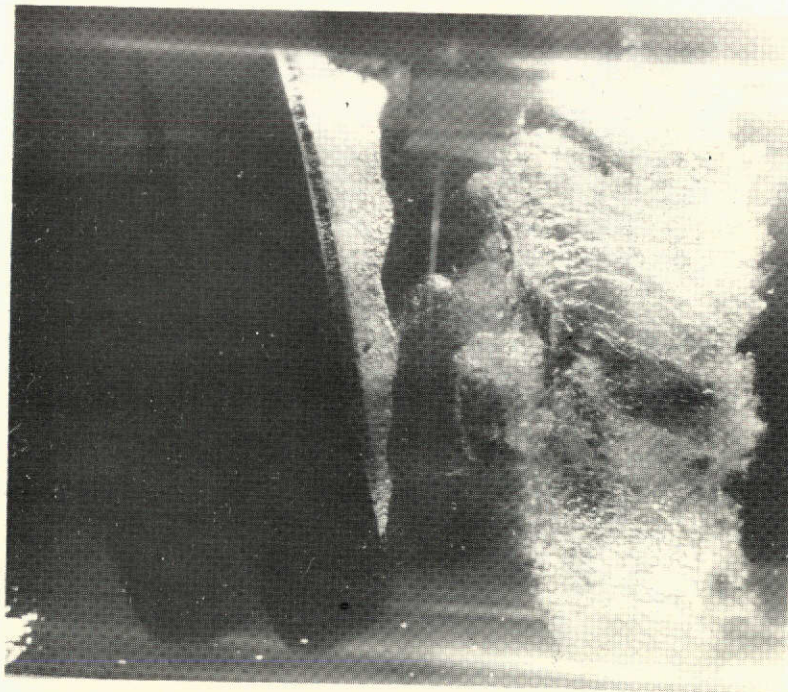
$\phi = .073 \quad N_{SS} = 4660$

FIGURE 28 - INFLUENCE OF FLOW COEFFICIENT ON CAVITATION PATTERNS AT LOW SUCTION SPECIFIC SPEED

C-2



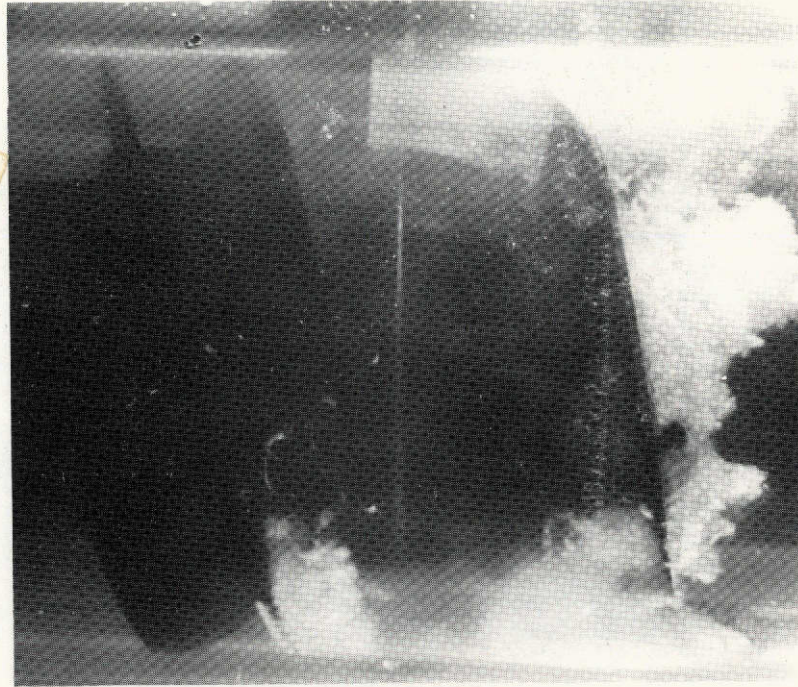
$$\phi = .0728 \quad N_{SS} = 12360$$



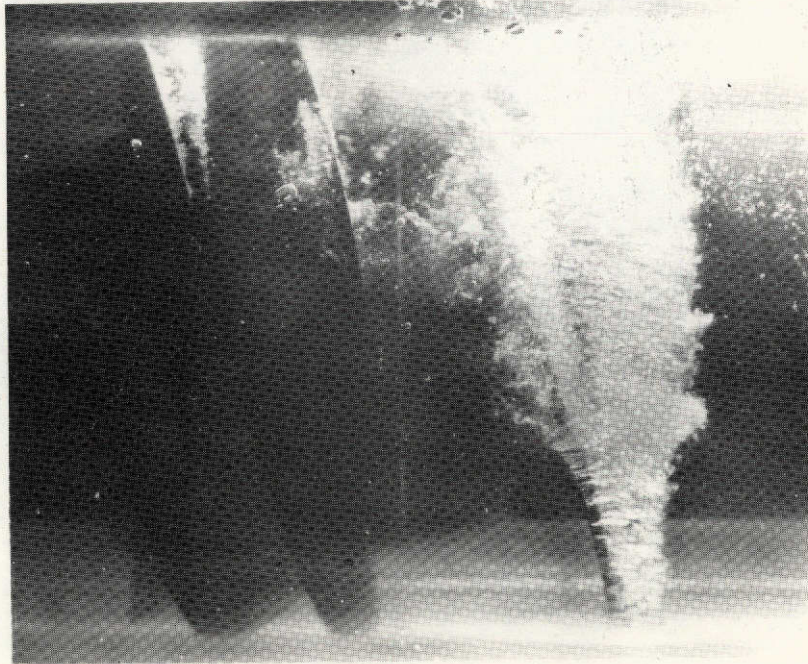
$$\phi = .0803 \quad N_{SS} = 15750$$

FIGURE 29 - CAVITATION PATTERNS AT MODERATE SUCTION SPECIFIC SPEEDS

Reproduced from
best available copy.

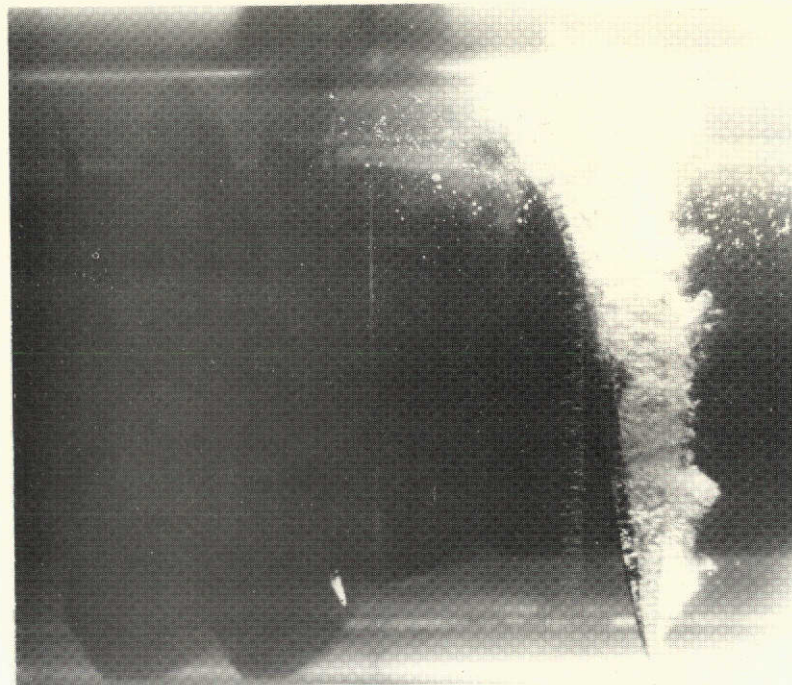


$$\phi = .0645 \quad N_{SS} = 20470$$

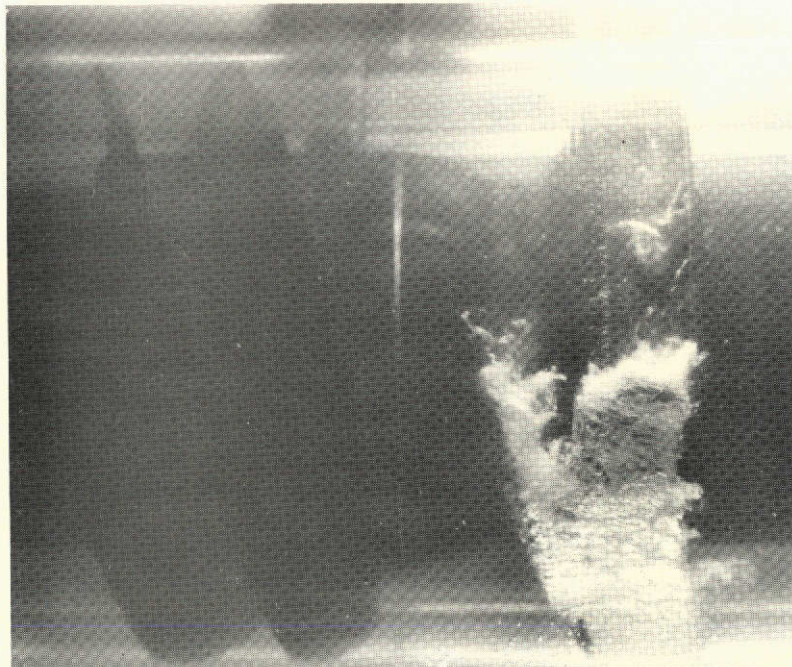


$$\phi = .0909 \quad N_{SS} = 21980$$

FIGURE 30 - CAVITATION PATTERNS AT HIGH SUCTION SPECIFIC SPEEDS

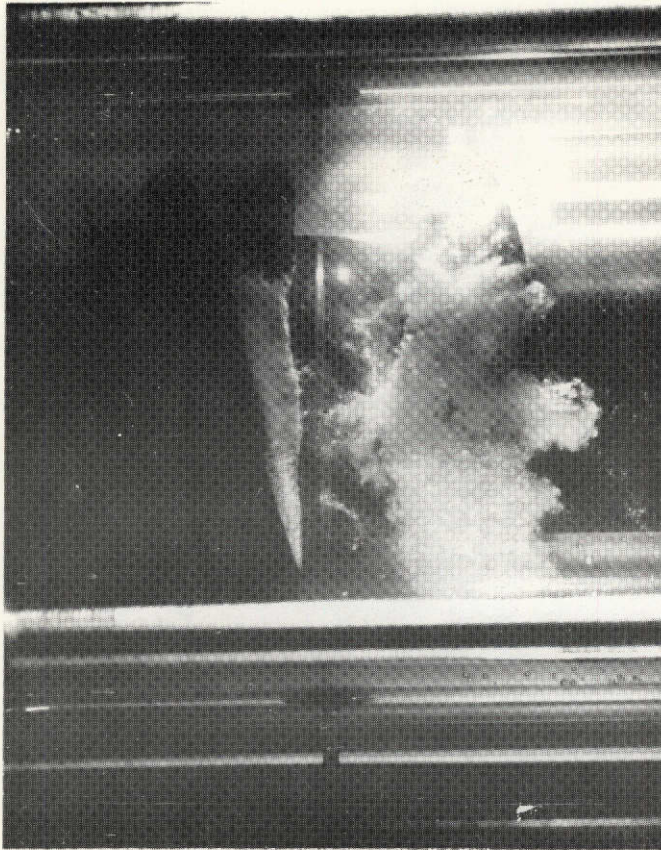


(a) LEADING EDGE OF CAVITY



(b) TRAILING EDGE OF CAVITY

FIGURE 31 - TWO VIEWS OF CAVITATION PATTERNS AT $\phi = .089$,
 $N_{SS} = 13430$ AT TWO ROTATIONAL ORIENTATIONS
ABOUT 90° APART



(a)



(b)

FIGURE 32 - ALTERNATE BLADE CAVITATION ON SECOND STAGE, $\phi = .0745$, $N_{SS} = 20,500$

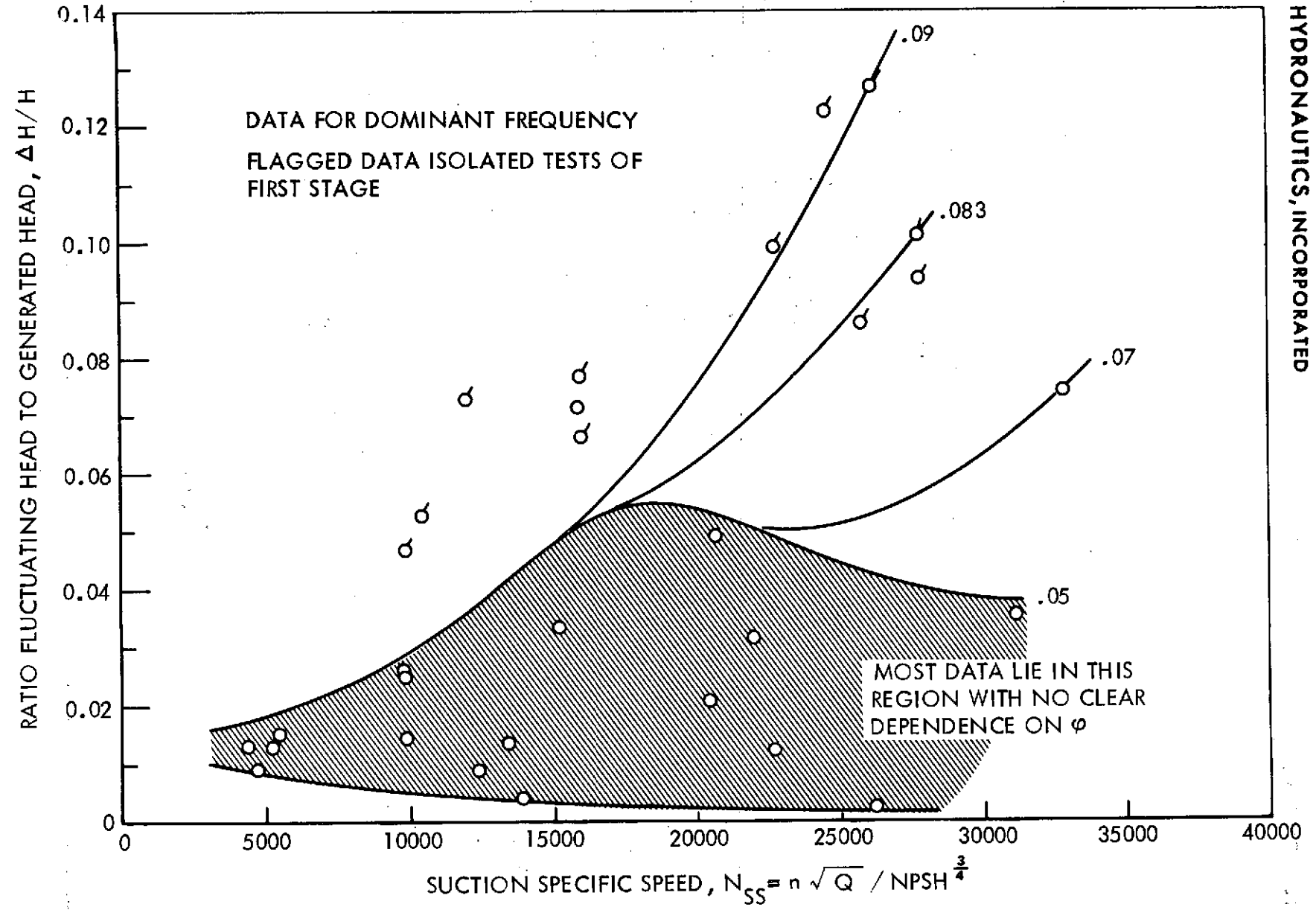


FIGURE 33 - RATIO OF FLUCTUATING TO STEADY HEAD DEVELOPED BY STAGE 1 AS INFLUENCED BY SUCTION SPECIFIC SPEED AND FLOW COEFFICIENT

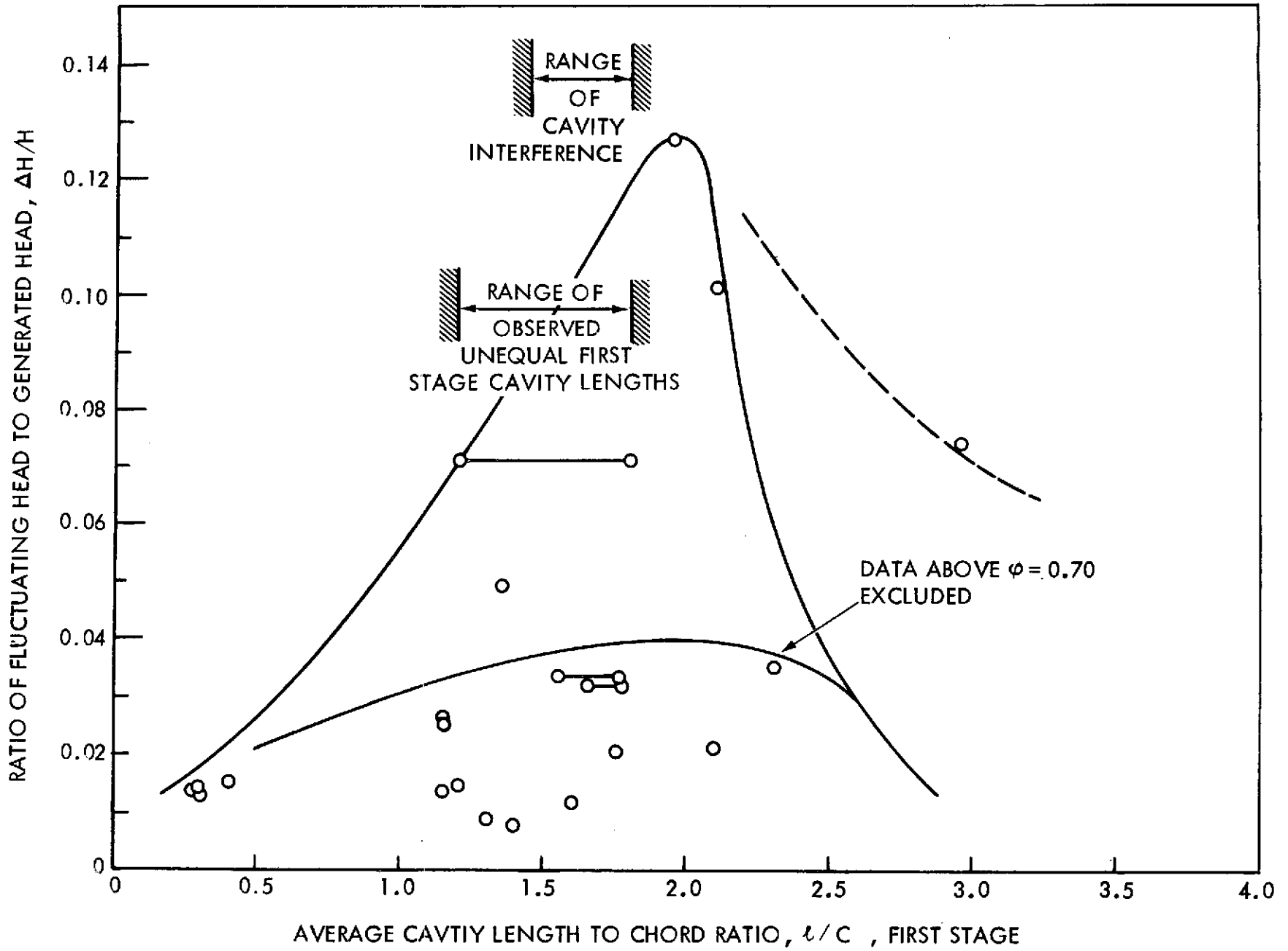


FIGURE 34 - INFLUENCE OF CAVITY LENGTH TO CHORD RATIO ON FLUCTUATING HEAD GENERATION

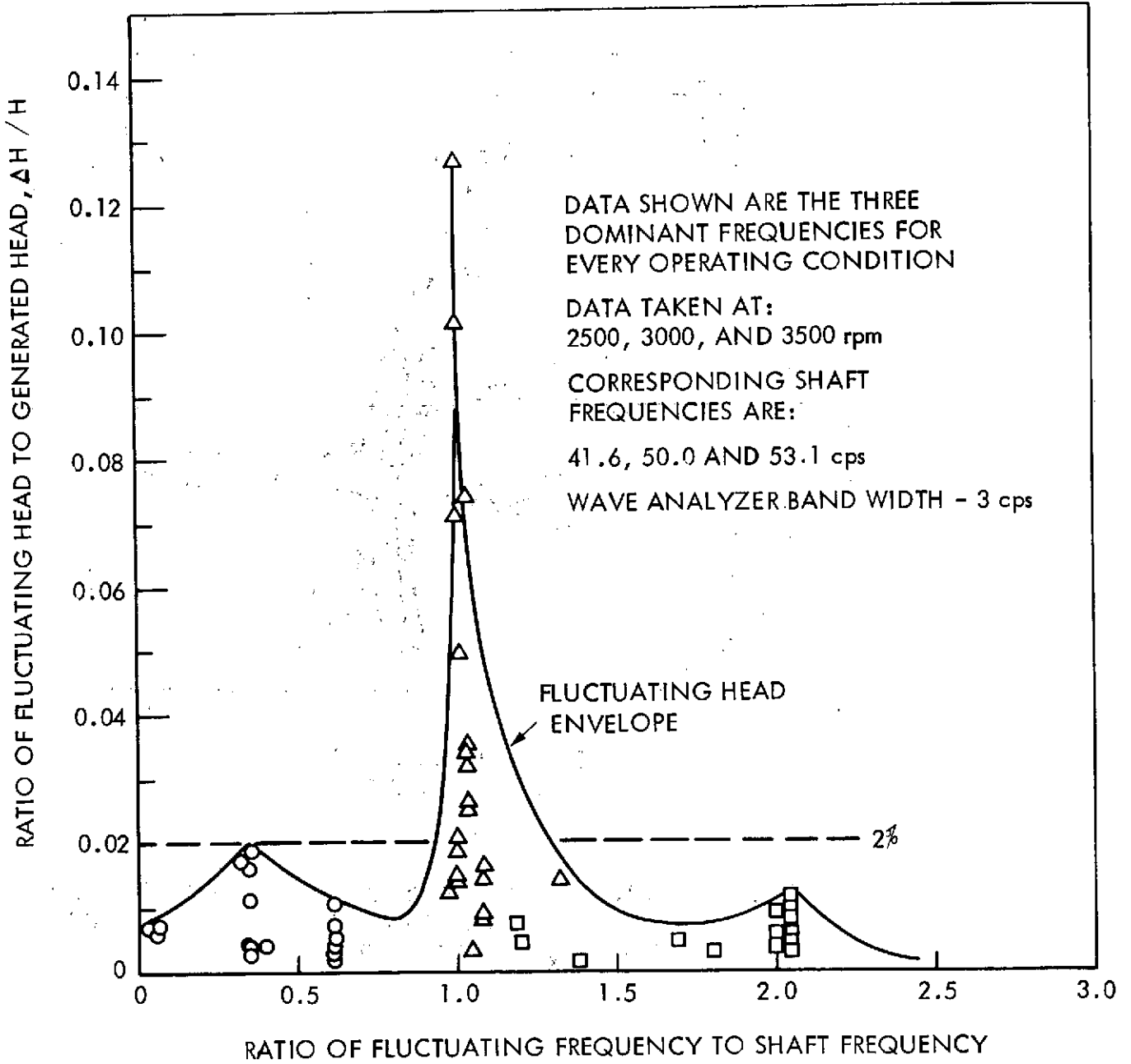


FIGURE 35 - LOW FREQUENCY FLUCTUATING HEAD SPECTRUM

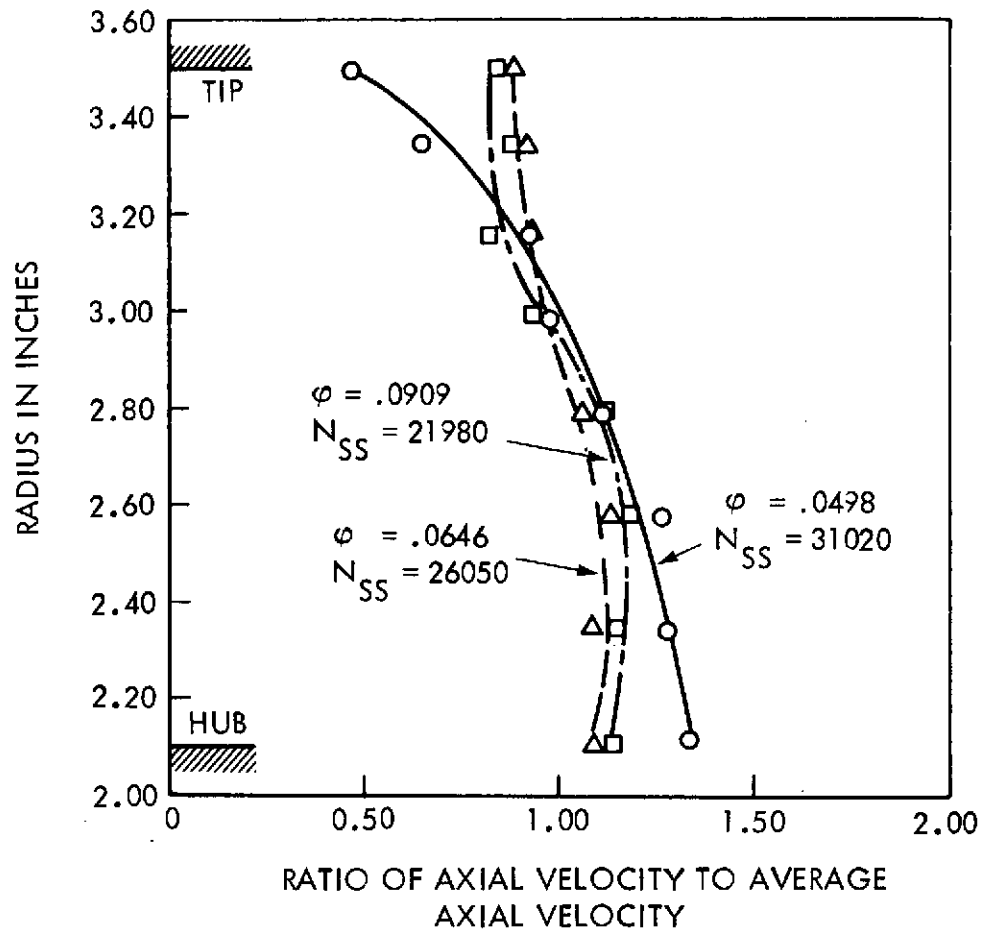


FIGURE 36 - UNIFORMITY OF AXIAL VELOCITY PROFILE EXISTING FROM STAGE 1 FOR VARYING FLOW COEFFICIENT AT HIGH SUCTION SPECIFIC SPEED

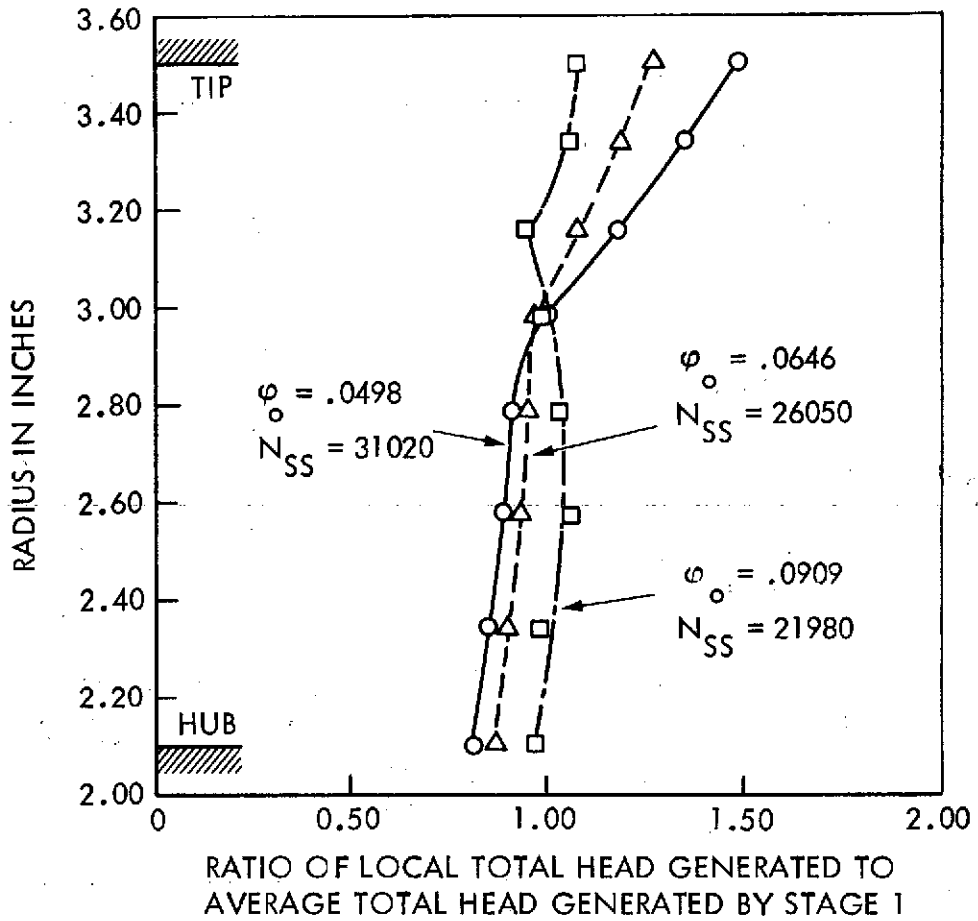


FIGURE 37 - UNIFORMITY OF HEAD GENERATION WITH RADIUS FOR STAGE 1 FOR VARYING FLOW COEFFICIENT AT HIGH SUCTION SPECIFIC SPEED

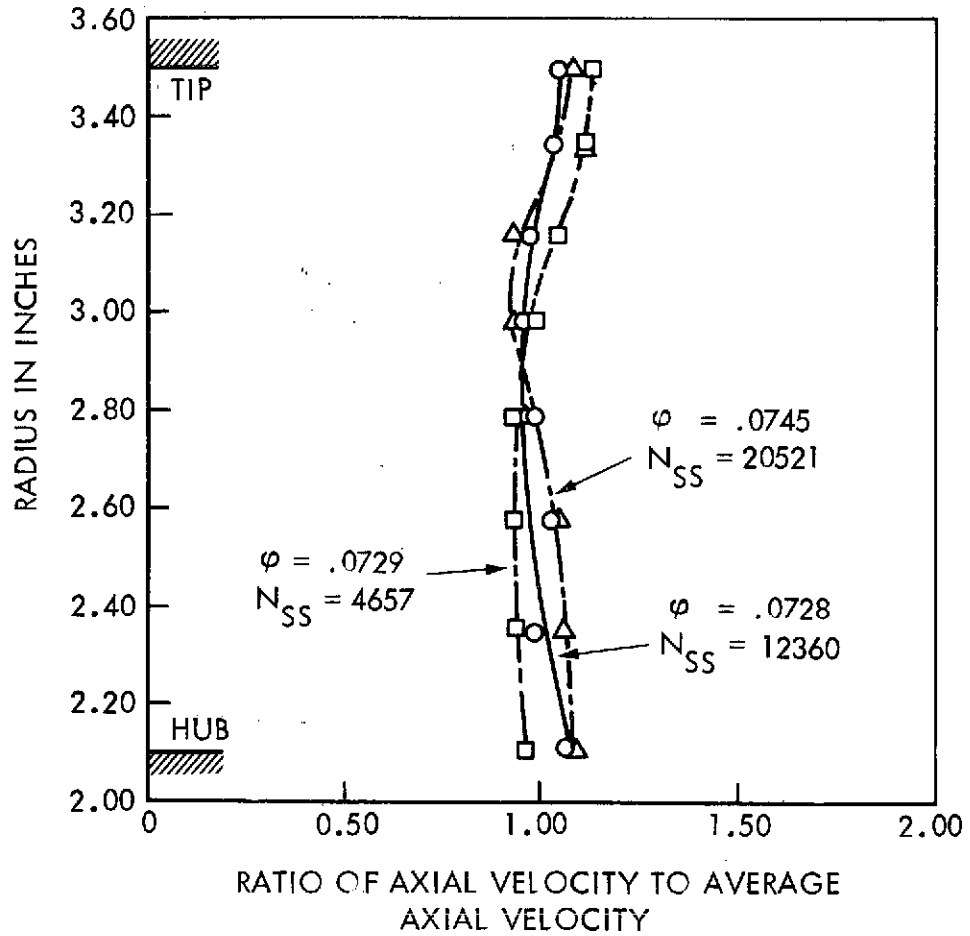


FIGURE 38 - UNIFORMITY OF AXIAL VELOCITY PROFILE EXITING FROM STAGE 1 FOR A WIDE RANGE OF SUCTION SPECIFIC SPEED AT NEARLY CONSTANT ϕ

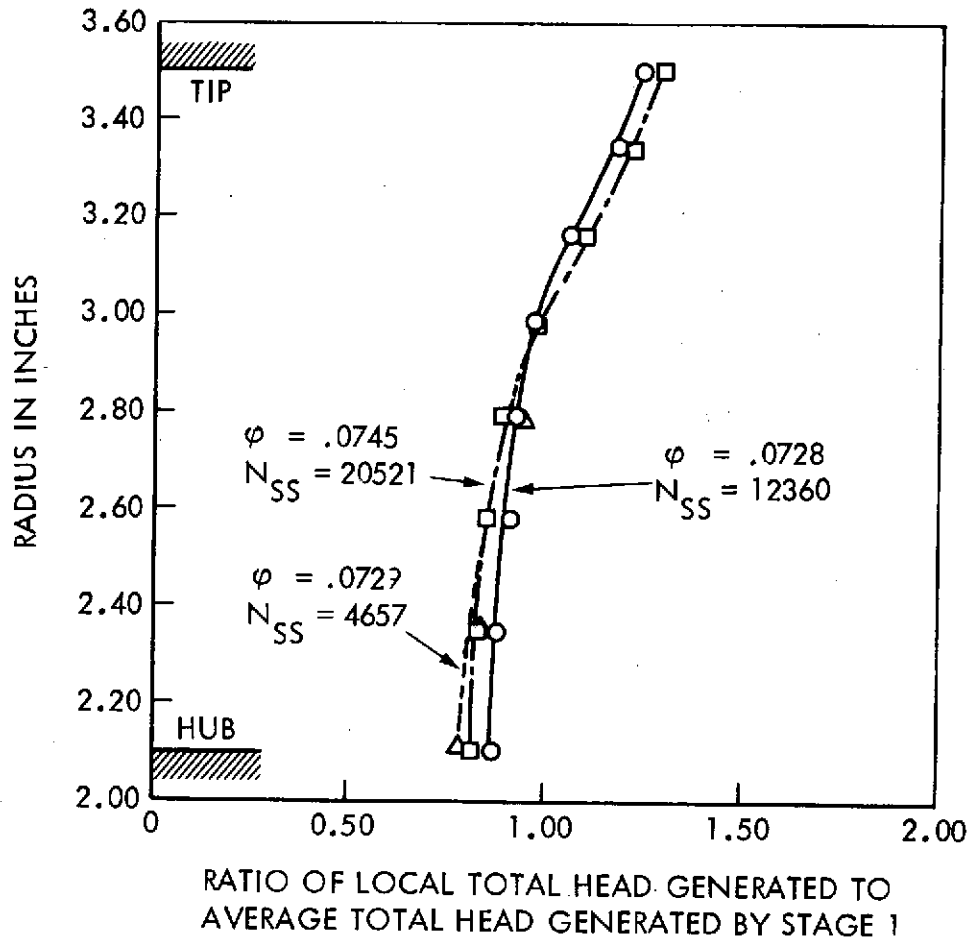


FIGURE 39 - UNIFORMITY OF HEAD GENERATION WITH RADIUS FOR STAGE 1 FOR A WIDE RANGE OF SUCTION SPECIFIC SPEED AT NEARLY CONSTANT ϕ

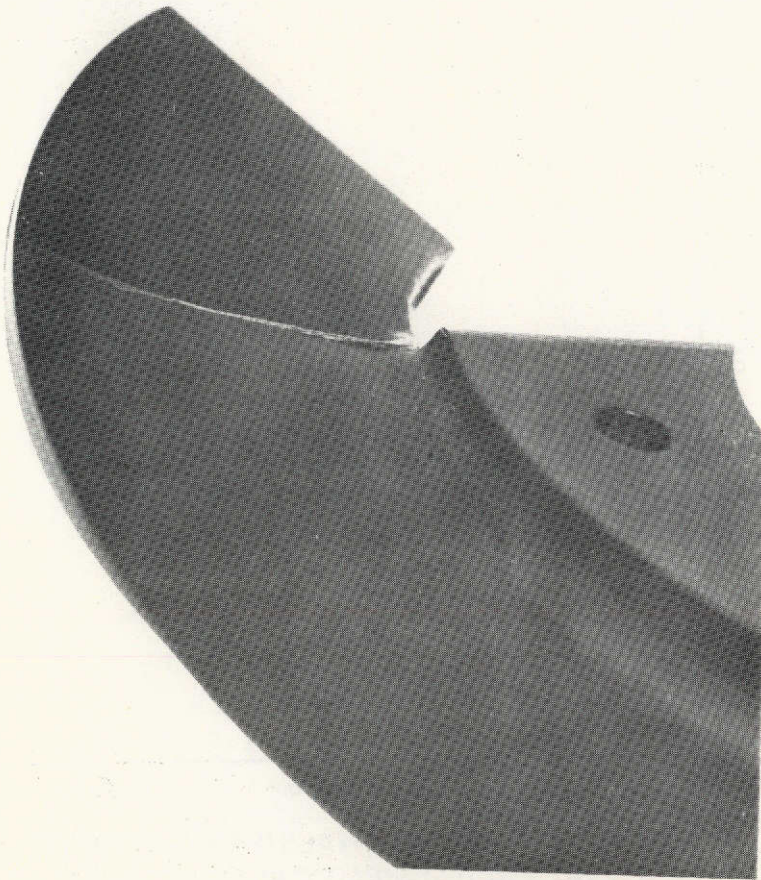
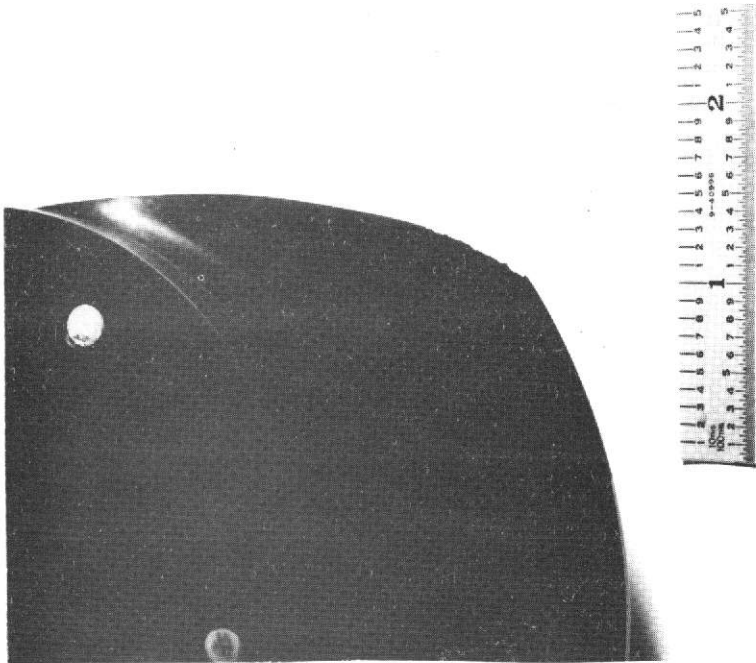
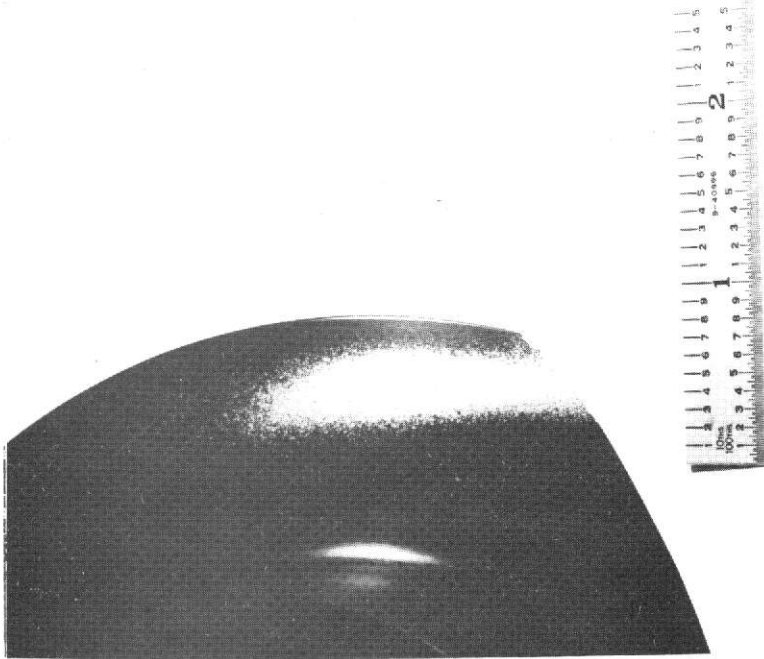


FIGURE 40 - INDUCER BLADE WITH TRAILING EDGE CRACK DUE TO
CANTILEVERED MODEL CONSTRUCTION



(a) BLADE BACK



(b) BLADE FACE

FIGURE 41 - LEADING EDGE DAMAGE TO STAGE 1